Hopping Around: Development of Methods for the Simulation of Non-Adiabatic Dynamics in Large Molecular Systems

Sean A. Fischer

A dissertation
submitted in partial fulfillment of the
requirements for the degree of

Doctor of Philosophy

University of Washington

2013

Reading Committee:

Xiaosong Li, Chair

Bo Zhang

David Masiello

Program Authorized to Offer Degree:
Chemistry

University of Washington

Abstract

Hopping Around: Development of Methods for the Simulation of Non-Adiabatic Dynamics in Large Molecular Systems

Sean A. Fischer

Chair of the Supervisory Committee:
Associate Professor Xiaosong Li
Department of Chemistry

Non-adiabatic molecular dynamics methods have been developed for the calculation of charge carrier dynamics, with a focus on large molecular and materials systems. These methods move beyond the Born-Oppenheimer approximation to account for transitions between electronic states. They are powerful companions to experimental measurements in elucidating chemical phenomena. In this dissertation we first give an overview of two of the most popular methods for non-adiabatic molecular dynamics: Ehrenfest dynamics and fewest switches surface hopping (FSSH). This is followed by a description of our implementation of FSSH within a single determinant framework. We showcase our implementation by examining the relaxation dynamics in both a transition-metal-doped, semiconductor quantum dot and a set of monomer units of conjugated polymers that serve as the electron donor phase of organic solar cells. We conclude with our development of a novel non-adiabatic molecular dynamics method, surface hopping with Ehrenfest excited potential (SHEEP). SHEEP was inspired by the electronic structure of systems like our semiconductor examples and is a combination of the non-adiabatic methods described in the opening chapter. It has performed well on a series of model problems, and it has the potential for significant computational savings over the FSSH method.

TABLE OF CONTENTS

Page

List of Figures iii

Glossary vii

Chapter 1: Introduction 1
1.1 Born-Oppenheimer molecular dynamics 2
1.2 Ehrenfest dynamics 3
1.3 Trajectory surface hopping 5

Chapter 2: Implementation of FSSH within a single determinant framework 10
2.1 Theory 10
2.2 Validation of single determinant approach 12
2.3 Computational savings through the classical path approximation . . . 14

Chapter 3: Charge transfer state formation in a Mn-doped ZnO quantum dot 16
3.1 Motivation and set-up 16
3.2 Relaxation dynamics 19

Chapter 4: Exciton relaxation dynamics of a series of conjugated copolymers 25
4.1 Motivation and set-up 25
4.2 Relaxation dynamics 27

Chapter 5: Surface hopping with Ehrenfest excited potential 35
5.1 SHEEP theory 35
5.2 Model problems 39
5.3 Boltzmann equilibrium populations 51
5.4 Approximations for SHEEP 57

Bibliography 61

Appendix A: Derivation of Ehrenfest dynamics 71

Appendix B: Derivation of FSSH 74

Appendix C: Fortran source code 77

LIST OF FIGURES

Figure Number Page

1.1 Schematic representation of the potential the nuclei "see" under Ehrenfest dynamics. The top panel shows all of the adiabatic potentials for the system. The bottom panel represents the average potential on which the nuclei would move under Ehrenfest dynamics. 4

1.2 Schematic representation of the potentials experienced by the nuclei under FSSH. Note, there is no difference between the top and bottom panels, i.e. the nuclei have the full set of PESs of the system to explore. 6

2.1 The first 19 excited state energies (referenced to the ground state) for a $Si_{29}H_{24}$ quantum dot calculated with LR-TDDFT (red lines) and KS orbital energy differences (blue dashes). The B3LYP exchange-correlation functional was used along with the 6-31G(d,p) basis set for the hydrogens and valence Si electrons, while the LANL2DZ pseudopotential was utilized for the core Si electrons. The energies were calculated with Gaussian [32] 13

3.1 Structure of the Mn-doped ZnO QD. The Mn atom is represented by the green sphere, the Zn atoms are represented by the blue segments, the O atoms are represent by the red segments, and the pseudo-H atoms are give by the white spheres. 17

3.2 Schematic representation of the charge transfer dynamics of interest. After exciting a band-to-band transition in the ZnO QD, a metal-to-ligand charge transfer occurs whereby the hole relaxes into the Mn^{2+} $3d$ levels, creating a Mn^{3+} species. 18

3.3 Isosurface plots of the HOMO and LUMO of our Mn^{2+}ZnO QD in the optimized ground state geometry. The HOMO shows significant localization around the Mn atom, while the LUMO is delocalized across the QD core. 20

3.4 Excitation energies as a function of time for the first 99 excited states. The $ML_{CB}CT$ states are marked in blue. 21

3.5 Calculated absorption spectrum for our QD. The red sticks are the calculated oscillator strengths for the first 99 excited states over the first 200 time steps of the BOMD trajectory. The blue line was computed by fitting a Gaussian function to each stick and summing the contributions at every energy. We used a width of 0.16 eV, which corresponds to the experimental broadening of the absorption spectrum. The blue line has been scaled down in order to fit on the same plot as the oscillator strengths. 22

3.6 Relaxation dynamics of the Mn-doped ZnO QD at 300 K. Displayed are the ground state population (red line) and $ML_{CB}CT$ state population (blue line). The inset shows the early time dynamics of the $ML_{CB}CT$ state. 23

3.7 Relaxation dynamics of the Mn-doped ZnO QD at 1 K. Displayed are the ground state population (red line) and $ML_{CB}CT$ state population (blue line). 24

4.1 Structure of the three monomer units that were studied. 27

4.2 HOMOs and LUMOs for the studied monomers. The HOMOs are all localized along the backbone of the monomer while the LUMOs are localized on the phanQ units. 28

4.3 Excitation energies over the course of the BOMD trajectories for the three monomers. The lowest excited state is highlighted in blue. . . . 29

4.4 Calculated absorption spectra for our three monomers. The lines were calculated in the same manner as before for the ZnO QD: a Gaussian function of width 0.13 eV (estimated broadening from the experimental spectrum for P1) was fit to each calculated oscillator strength (not shown), and the contributions were summed at every energy. Absorption spectra from 200 different nuclear configurations were sampled for each line. Monomer P1 is given by the solid, red line, P2 is the dotted, blue line, and P3 is the dashed, green line. 30

4.5 Relaxation dynamics for our three monomers. The starting electronic state was the first excited state (highlighted region on the inset absorption spectra), and displayed is the population of that state. Monomer P1 is given by the solid, red line, P2 is the dotted, blue line, and P3 is the dashed, green line. 31

4.6 First excited state population as a function of time for the three monomers. The starting electronic state here was the state with the high oscillator strength under the second peak in the absorption spectra (highlighted region on the inset absorption spectra). Monomer P1 is given by the solid, red line, P2 is the dotted, blue line, and P3 is the dashed, green line. 32

4.7 Average magnitude of the non-adiabatic coupling between the first excited state and the ground state over the first 100 fs of the trajectories beginning from each initial condition. 33

5.1 Schematic representation of SHEEP. The ground state remains unaltered while all of the excited states are folded into a single, average excited state. 36

5.2 Three states with multiple avoided crossings model. Top panel: Adiabatic potential energy curves as a function of the nuclear coordinate. Bottom panel: Non-adiabatic coupling strengths between adiabatic states as a function of the nuclear coordinate. 40

5.3 Three states with multiple avoided crossings model. (a) Probability of transmission on the ground adiabatic state. (b) Probability of reflection on the ground adiabatic state. (c) Probability of transmission on the excited adiabatic states. Blue circles are the SHEEP results, FSSH is given by red squares, and MF is given by black triangles. 42

5.4 Three states with multiple avoided crossings model. (a) Probability of transmission on the first excited adiabatic state. (b) Probability of transmission on the second excited adiabatic state. 43

5.5 Harmonic oscillator with equally spaced excited states model. Adiabatic potential energy curves as a function of the nuclear coordinate. The circle shows the initial position for the trajectories. 44

5.6 Harmonic oscillator with equally spaced excited states model. Time evolution of the ground state population. Loss of coherence between members of the ensembles causes the dampening of the oscillations for the surface hopping results. 45

5.7 Harmonic oscillator with equally spaced excited states model. Time evolution of the average momentum (top panel) and position (bottom panel) of the heavy particle. Spreading of the trajectories in phase space causes the approach of the averages towards zero for SHEEP and FSSH. 46

5.8 Harmonic oscillator with a dense manifold of excited states model. Adiabatic potential energy curves as a function of the nuclear coordinate. The circle shows the initial position for the trajectories. 47
5.9 Harmonic oscillator with a dense manifold of excited states model. Time evolution of the ground state population. Bringing the excited states closer together brings the SHEEP and FSSH results closer together. 48
5.10 Harmonic oscillator with a dense manifold of excited states model. Time evolution of the average momentum (top panel) and position (bottom panel) of the heavy particle. 49
5.11 Thirty states with avoided crossings model. (a) Diabatic potential energy curves as a function of nuclear coordinate. (b) Adiabatic potential energy curves as a function of the nuclear coordinate. 50
5.12 Thirty states with avoided crossings model. Probability of transmission on the ground adiabatic state as a function of initial momentum. . . . 51
5.13 Ground state population as a function of temperature. The red line is the Boltzmann result, the black squares are the FSSH results, and the blue circles are the SHEEP results. The error bars represent the standard deviations of the population averages. 54
5.14 Ground state population as a function of temperature. The red line is the Boltzmann result, the black squares are the FSSH results, the blue circles are the SHEEP results, and the gray diamonds are the modified FSSH results. The error bars represent the standard deviations of the population averages. 56
5.15 Ground state population as a function of temperature. The red line is the Boltzmann result, the blue circles are the SHEEP results, and the green triangles are the modified SHEEP results. The error bars represent the standard deviations of the population averages. 59

GLOSSARY

MOLECULAR DYNAMICS: Numerical simulation of the motion of, generally, classical atoms.

ADIABATIC MOLECULAR DYNAMICS: Molecular dynamics confined to a single potential energy surface with no transitions between surfaces

NON-ADIABATIC MOLECULAR DYNAMICS: Molecular dynamics where transitions between potential energy surfaces are taken into account

ACKNOWLEDGMENTS

I would like to acknowledge the advisors who have guided me along my journey: Xiaosong Li, Oleg Prezhdo, and Sergei Tretiak. Additionally, I would like to acknowledge the support of all my fellow graduate students in the Theory Suite.

DEDICATION

To my always wonderful wife and my sometimes daft dog.

Chapter 1

INTRODUCTION

As chemists, the Born-Oppenheimer (BO) approximation [11] largely shapes how we view the world around us. It provides backing for the ubiquitous ball and stick representation of molecular structures and underlies the idea of a potential energy surface (PES). The fundamental aspect of the BO approximation is the separation of nuclear and electronic motions based upon the substantial difference in mass between electrons and nuclei. Uncoupling these motions results in a great simplification of the molecular problem. We first solve for the configuration of the electrons assuming the nuclei are stationary. This step generates a PES that is a function of the nuclear coordinates. It is upon this PES that we then propagate the nuclei. Often additional computational savings are made by neglecting the quantum nature of the nuclei and employing a classical description. Much can be learned through a dynamical exploration of this PES, with simulated dynamics being a powerful companion to experimental probing.

The BO approximation remains valid only if there is significant separation between the electronic energy levels calculated in the first step mentioned above (here we define a significant separation to be one where the difference in electronic energy is much greater than the kinetic energy available to the system). However, even when the BO approximation begins to breakdown, it still influences the description of those phenomena which are beyond its range of rigorous applicability. Non-radiative transitions in molecular systems are often thought of in terms of transitions between BO electronic states, even though the BO approximation is not valid here. In these cases a BO-based theory can be extended to account for these non-adiabatic effects

by including multiple electronic states and the coupling between them that is induced via the nuclear motion.

1.1 Born-Oppenheimer molecular dynamics

Molecular dynamics is the numerical simulation of the motion of atoms and molecules. The entirety of molecular dynamics is a vast field ranging from the coarse-grained simulation of entire proteins to the fully quantum mechanical treatment of small molecules. The focus here will remain on the small subset known as *ab initio* molecular dynamics (AIMD). AIMD generally treats nuclei as classical point particles moving on PESs calculated via quantum mechanics. The most well known method under this heading is BO molecular dynamics (BOMD). For BOMD the nuclei of a molecule are propagated along the ground electronic state of the system.

From a mathematical point-of-view this is accomplished by first solving the time-independent Schrödinger equation,

$$\hat{\mathcal{H}}_{el}(\mathbf{r},\mathbf{R})\Phi_0(\mathbf{r};\mathbf{R}) = \mathcal{E}_0(\mathbf{R})\Phi_0(\mathbf{r};\mathbf{R}) \tag{1.1}$$

where $\mathbf{r}$ and $\mathbf{R}$ represent electronic and nuclear coordinates, respectively. The Hamiltonian in Eq. 1.1 is the electronic Hamiltonian for fixed nuclei and is given as,

$$\hat{\mathcal{H}}_{el}(\mathbf{r},\mathbf{R}) = -\frac{\hbar^2}{2m_e}\nabla^2_{\mathbf{R}} + V(\mathbf{r},\mathbf{R}). \tag{1.2}$$

The first term is the electronic kinetic energy operator with electron mass m_e, the second term is includes all particle-particle interactions. The adiabatic electronic wave functions Φ_k are the solutions to the time-independent Schrödinger equation given in Eq. 1.1, where we have restricted ourselves to only the ground state for now. The eigenvalues corresponding to these eigenfunctions are the adiabatic PESs. For BOMD we will only be concerned with that of the ground electronic state $\mathcal{E}_0$.

Once the electronic energy is found for the current nuclear configuration, its gradient with respect to the nuclear coordinates is used to advance the positions of the

nuclei according to Newton's equation of motion:

$$M\ddot{\mathbf{R}} = -\nabla_{\mathbf{R}}\mathcal{E}_0(\mathbf{R}). \tag{1.3}$$

This process is repeated until the desired simulation time has been reached. The advantage of this approach is that a relatively large time step can be used for propagation since the nuclear coordinates are the only ones being propagated in time. The disadvantages consist of the necessity to converge the electronic wave function at every time step and, more importantly, the restriction to motion on the ground electronic state.

To explore some of the more interesting chemical phenomena, we will need to be able to account for motion on other electronic states and for transitions between states. Various methods have been introduced to move dynamics beyond the BO approximation; [60, 73, 86, 67, 62, 41, 63, 65, 64, 82, 91, 59, 79, 75, 9, 55, 66, 19, 10, 95, 8] however, we will focus on those that retain the classical description of nuclear motion that underlies the ability of such approaches to treat relatively large systems in full dimensionality.

1.2 Ehrenfest dynamics

Conceptually straightforward and one of the earliest approaches for moving beyond BOMD, Ehrenfest dynamics is based on a mean-field separation of nuclear and electronic motion. Physically, Ehrenfest dynamics involves propagating the nuclei on a mean potential energy surface that is constructed from the expectation value of the total electronic energy (see Fig. 1.1). Mathematically, the method can be derived as a partial classical limit of the time-dependent self-consistent field (TDSCF) method (see appendix for a derivation). [33, 84, 55] In the end we obtain a classical equation of motion for the nuclei,

$$M\ddot{\mathbf{R}} = -\nabla_{\mathbf{R}} \left\langle \Theta(\mathbf{r},t;\mathbf{R}) \left| \hat{\mathcal{H}}_{el}(\mathbf{r},\mathbf{R}) \right| \Theta(\mathbf{r},t;\mathbf{R}) \right\rangle_{\mathbf{r}}, \tag{1.4}$$

while the electronic degrees of freedom are governed by the time-dependent electronic Schrödinger equation:

$$i\hbar\frac{\partial}{\partial t}\Theta(\mathbf{r},t;\mathbf{R}) = \hat{\mathcal{H}}_{el}(\mathbf{r},\mathbf{R})\Theta(\mathbf{r},t;\mathbf{R}). \tag{1.5}$$

In Eqs. 1.4 and 1.5 the total electronic wave function is given by Θ, which has a parametric dependence on the nuclear coordinates. Here and throughout, the brackets indicate integration over the subscripted coordinates.

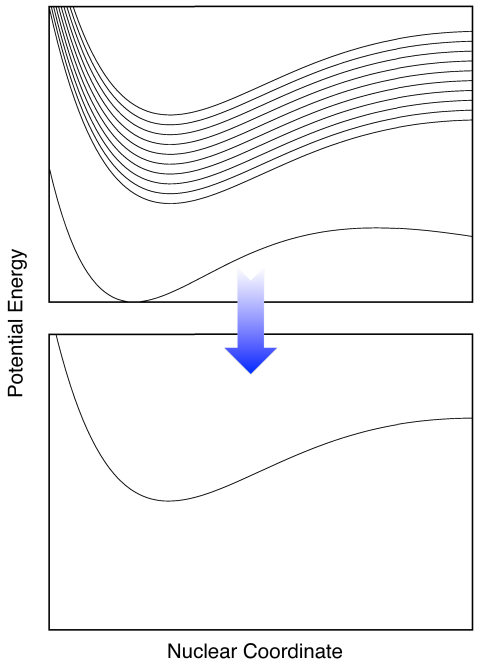

Figure 1.1: Schematic representation of the potential the nuclei "see" under Ehrenfest dynamics. The top panel shows all of the adiabatic potentials for the system. The bottom panel represents the average potential on which the nuclei would move under Ehrenfest dynamics.

The Ehrenfest method conserves total energy while allowing for energy transfer between the nuclear and electronic subsystems. Additionally, the Ehrenfest approach

gives exact results for the expectation values of quantum observables when the potentials are no more than quadratic functions of the coordinates. [52] Ehrenfest dynamics also benefits from not requiring explicit computations of excited states. However, explicit correlations between nuclear and electronic motions are absent, and the restriction to an average potential energy surface can lead to unphysical results after the system leaves a region of coupling between the electronic states. [82, 33]

Another area where the Ehrenfest method falls short is obtaining correct equilibrium distributions for the quantum state populations. [70] To obtain quantum state populations for Ehrenfest dynamics, we expand the total electronic wave function in a basis and take the square of the expansion coefficients for each basis state. This shortcoming of Ehrenfest can be understood by considering the ansatz for the total wave function that was used in deriving the method. In order to obtain a relatively simple set of equations for the dynamics of our system, we began by assuming that the electronic wave function was independent of the nuclear coordinates. This assumption will only be true if there is no coupling between states, or we are at high temperatures. It is this high temperature behavior that is seen when looking at the equilibrium populations of the quantum states with Ehrenfest dynamics; for all temperatures Ehrenfest dynamics results in near equal population of all quantum states.

1.3 Trajectory surface hopping

Trajectory surface hopping is a method that was developed specifically to account for correlations between nuclear and electronic motions. We focus on Tully's fewest switches version of trajectory surface hopping [82] as it is the most popular and generally applicable. Fewest switches surface hopping (FSSH) propagates the nuclei classically along the potential energy surface of a single electronic basis state but allows for stochastic transitions between basis states any time the coupling is sufficient. In a sense the nuclei experience the potentials of all the basis states as opposed to Ehrenfest where there is only a single average potential for the nuclear propagation,

compare Figs. 1.1 and 1.2. The method can be derived as an approximation to the dynamics resulting from a multi-configuration expansion for the total wave function [83] (see appendix for this derivation).

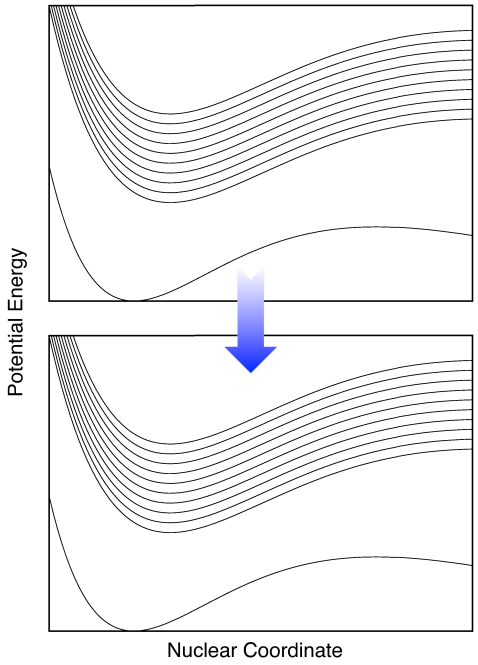

Figure 1.2: Schematic representation of the potentials experienced by the nuclei under FSSH. Note, there is no difference between the top and bottom panels, i.e. the nuclei have the full set of PESs of the system to explore.

A FSSH simulation proceeds by propagating the nuclei along the PES of one of the basis states:

$$M\ddot{\mathbf{R}} = -\nabla_{\mathbf{R}}\mathcal{E}_k(\mathbf{R}) \tag{1.6}$$

where k is the currently occupied basis state. At every time step, or every few time steps, a decision is made whether to move the dynamics to the PES of another basis state via comparison of a hopping probability with a random number. If a transition is predicted, then subsequent motion will continue on the new basis state

and the nuclear kinetic energy is adjusted in order to compensate for the change in electronic energy, so as to maintain total energy conservation. If there is insufficient nuclear kinetic energy to accommodate the change in electronic energy, then the transition is aborted and propagation continues along the previous state. Since the transitions between states are random, the final results need to be averaged over many surface hopping trajectories starting from the same initial conditions in order to obtain meaningful results.

There are many possibilities for determining hopping probabilities between states; FSSH makes use of the time-dependent electronic Schrödinger equation (Eq. 1.5) for that task. We first need to expand the total electronic wave function in a basis,

$$\Theta(\mathbf{r}, t; \mathbf{R}) = \sum_j c_j(t)\Phi_j(\mathbf{r}; \mathbf{R}). \tag{1.7}$$

The basis can be either adiabatic or diabatic; however, various arguments have been made in favor of the adiabatic basis. [83] Substituting this expansion into Eq. 1.5 leads to a set of equations for the time evolution of the expansion coefficients,

$$i\hbar\dot{c}_k(t) = \sum_j c_j(t)\left[H_{kj}(\mathbf{R}) - i\hbar\dot{\mathbf{R}}\cdot\mathbf{d}_{kj}(\mathbf{R})\right] \tag{1.8}$$

where the dot over the coefficient implies a time derivative and H_{kj} are the matrix elements of the electronic Hamiltonian and $\mathbf{d}_{kj}$ are the non-adiabatic couplings,

$$H_{kj}(\mathbf{R}) = \left\langle \Phi_k(\mathbf{r};\mathbf{R}) \left| \hat{\mathcal{H}}_{el}(\mathbf{r},\mathbf{R}) \right| \Phi_j(\mathbf{r};\mathbf{R}) \right\rangle_{\mathbf{r}} \tag{1.9}$$

$$\mathbf{d}_{kj}(\mathbf{R}) = \left\langle \Phi_k(\mathbf{r};\mathbf{R}) \left| \nabla_{\mathbf{R}}\Phi_j(\mathbf{r};\mathbf{R}) \right\rangle_{\mathbf{r}} \right. . \tag{1.10}$$

Equation 1.8 can be recast in terms of elements of the density matrix by defining $a_{kj} = c_k c_j^*$, thereby yielding

$$i\hbar\dot{a}_{kj}(t) = \sum_l \Big\{ a_{lj}(t)\left[H_{kl}(\mathbf{R}) - i\hbar\dot{\mathbf{R}}\cdot\mathbf{d}_{kl}(\mathbf{R})\right] - a_{kl}(t)\left[H_{lj}(\mathbf{R}) - i\hbar\dot{\mathbf{R}}\cdot\mathbf{d}_{lj}(\mathbf{R})\right]\Big\}. \tag{1.11}$$

From Eq. 1.11 it can be shown that the diagonal elements of the density matrix obey

$$\dot{a}_{kk}(t) = \sum_{l \neq k} b_{kl}(t) \tag{1.12}$$

$$b_{kl}(t) = \frac{2}{\hbar}\mathrm{Im}\left(a^*_{kl}(t)H_{kl}(\mathbf{R})\right) - 2\mathrm{Re}\left(a^*_{kl}(t)\dot{\mathbf{R}}\cdot\mathbf{d}_{kl}(\mathbf{R})\right). \tag{1.13}$$

The b_{kl} are the state-to-state transition probabilities and give rise to the hopping probabilities:

$$g_{kj} = \frac{\Delta t b_{jk}(t)}{a_{kk}(t)}. \tag{1.14}$$

If a hopping probability is calculated to be negative, it is set to zero. At each time step, the hopping probabilities for transitions from the current state k to all other states j are computed and compared with a number generated randomly from a uniform distribution on the interval $0 < \zeta < 1$. For example if the current state is 1, a switch to state 2 will occur if $\zeta < g_{12}$. A switch to state 3 will occur if $g_{12} < \zeta < g_{12} + g_{13}$, etc. If a switch is called for, the component of the nuclear momentum in the direction of the non-adiabatic coupling vector is scaled so as to conserve total energy. If the momentum is not sufficient to compensate for the change in electronic energy, then the hop is aborted and the sign of the momentum along the non-adiabatic coupling vector is changed. If no switch is called for (i.e. the random number is greater than all the hopping probabilities), then the propagation continues unchanged. Note, a state switch changes the identity of the basis state determining the forces on the nuclei (Eq. 1.6) and the potential energy of the system but does not directly modify the density matrix elements propagated with Eq. 1.11 and used in the determination of hopping probabilities.

The FSSH method has been shown to be rather accurate in small model systems [82, 70] and has been applied to a wide variety of chemical system. [27, 28] The method also has been shown to nearly satisfy detailed balance while the Ehrenfest method lacks this attribute. [70] Computationally, FSSH is more demanding than

Ehrenfest dynamics. Explicit excited state wave functions are required, and additional averaging is necessary because of the stochastic nature of the algorithm. Also, some work has shown the results of FSSH to be unreliable for problems involving long interaction times or repeated entries into the interaction region. [52, 68] Still surface hopping remains one of the most popular methods for the treatment of non-adiabatic chemical dynamics and forms the basis for the developments that we will discuss here.

Chapter 2

IMPLEMENTATION OF FSSH WITHIN A SINGLE DETERMINANT FRAMEWORK

The first project we will discuss is the development of our own implementation of FSSH. We have written our own FSSH code that interfaces with electronic structure calculations, giving us the ability to study the charge carrier dynamics of various chemical systems. This chapter details the theory behind the implementation, while the next two chapters give brief demonstrations of the capabilities of our new method.

Following the work of Prezhdo and co-workers, [21, 49] we have implemented FSSH within the framework of single determinant wave functions. This scheme has been successfully applied to a variety of systems: semiconductor quantum dots, [49, 50] carbon nanotubes, [38] graphene nanoribbons, [37] and semiconductor/molecular interfaces. [25, 27]

2.1 Theory

The time-dependent, electronic Schrödinger equation is the starting point for the electronic dynamics:

$$i\hbar\frac{\partial}{\partial t}\Theta(\mathbf{r},t;\mathbf{R}) = \hat{\mathcal{H}}_{el}(\mathbf{r},\mathbf{R},t)\Theta(\mathbf{r},t;\mathbf{R}). \tag{2.1}$$

In the above, we represent our electronic wave function in a basis of Slater determinants constructed from molecular orbitals (MOs),

$$\Theta(\mathbf{r},t;\mathbf{R}) = \sum_j c_j(t)\Phi_j(\mathbf{r};\mathbf{R}), \tag{2.2}$$

which are solutions to the Hartree-Fock (HF)/Kohn-Sham (KS) self-consistent field equations. The Slater determinant is the simplest approximation to the electronic

wave function that satisfies the anti-symmetry requirement for fermions. In HF theory the use of a Slater determinant results in the motion of electrons of the same spin being correlated, while there is no correlation between electrons of opposite spins. The KS equations account for both the correlation between electrons of the same spin (exchange energy) and the correlation between electrons of opposite spins (correlation energy) in an approximate way. The Slater determinant will be a good approximation to a given electronic wave function when a single electronic configuration dominates for that state, e.g. no degeneracies and little correlation energy.

The ground state determinant (Φ_0) is formed from the lowest energy MOs, while the excited state determinants are formed via single substitutions from the ground state determinant. In general our MOs will not be orthonormal; consequently, our determinant wave functions will also not be orthonormal. We remedy this through a Löwdin orthogonalization and normalization procedure. [57]

We can insert the expansion into the time-dependent equation to obtain the evolution of the expansion coefficients:

$$i\hbar\dot{c}_k(t) = \sum_j^{N_{ad}} c_j(t) \left(H_{kj}(\mathbf{R})\delta_{kj} - i\hbar\dot{\mathbf{R}} \cdot \mathbf{d}_{kj}(\mathbf{R}) \right), \tag{2.3}$$

where the summation is truncated at N_{ad} adiabatic states. The adiabatic state energies $H_{jj} = \langle \Phi_j | \hat{\mathcal{H}}_{el} | \Phi_j \rangle_{\mathbf{r}}$ can be referenced to the ground state, allowing us to replace H_{jj} with MO energy differences,

$$\tilde{H}_{jj}(\mathbf{R}) = \epsilon_q(\mathbf{R}) - \epsilon_a(\mathbf{R}) = H_{jj}(\mathbf{R}) - H_{00}(\mathbf{R}) \tag{2.4}$$

where ϵ_q and ϵ_a represent the MOs substituted into and out of the reference determinant in order to form the j-th excited state. The non-adiabatic couplings are non-zero only if the Slater determinants differ in a single orbital:

$$\begin{aligned} \mathbf{d}_{jk}(\mathbf{R}) &= \langle \Phi_j(\mathbf{r};\mathbf{R}) \left| \nabla_{\mathbf{R}} \Phi_k(\mathbf{r};\mathbf{R}) \right\rangle_{\mathbf{r}} \\ &= \langle \phi_q(\mathbf{r};\mathbf{R}) \left| \nabla_{\mathbf{R}} \phi_s(\mathbf{r};\mathbf{R}) \right\rangle_{\mathbf{r}} \delta_{ab} - \langle \phi_a(\mathbf{r};\mathbf{R}) \left| \nabla_{\mathbf{R}} \phi_b(\mathbf{r};\mathbf{R}) \right\rangle_{\mathbf{r}} \delta_{qs}, \end{aligned} \tag{2.5}$$

where δ_{ab} is the Kronecker delta. The hopping probabilities are calculated the like before,

$$g_{kj} = \frac{-2\Delta t \mathrm{Re}\left(c_j^*(t)c_k(t)\dot{\mathbf{R}}\cdot\mathbf{d}_{jk}(\mathbf{R})\right)}{c_k(t)c_k^*(t)}. \tag{2.6}$$

These hopping probabilities are tested against a uniform random number to determine if a transition to another state will occur at a given time step.

2.2 Validation of single determinant approach

The use of single Slater determinants as the basis for our dynamics is a computationally efficient choice but also a potentially severe approximation. [58, 80] In general, excitation energies calculated via MO energy differences will not agree with the true excitation energies of the system. This also means that the forces obtained from a single determinant reference will not generally agree with the true forces. Implementation of surface hopping methods with more accurate electronic structure methods is certainly possible and has been done by others. [80, 88, 72] However, increasing the accuracy of your electronic structure method generally goes hand-in-hand with decreasing the size of the system for which you can perform the calculation. Our interests lie in studying large systems such as quantum dots, where correlated wave function methods and even linear-response density functional methods become prohibitively expense in terms of dynamical simulations.

Fortuitously, when working with these large systems the single determinant framework becomes a reasonable approximation. We previously analyzed the performance of the KS formalism of density functional theory (DFT) as compared with the results of linear-response, time-dependent DFT (LR-TDDFT). [28] We found that for the systems in which we are interested in studying, the KS excitations provide a good approximation with the LR-TDDFT values. This is demonstrated in Fig. 2.1 where we calculated excitation energies along a sample portion of MD trajectory for a $Si_{29}H_{24}$ quantum dot. Given are both the excitation energies found via LR-TDDFT

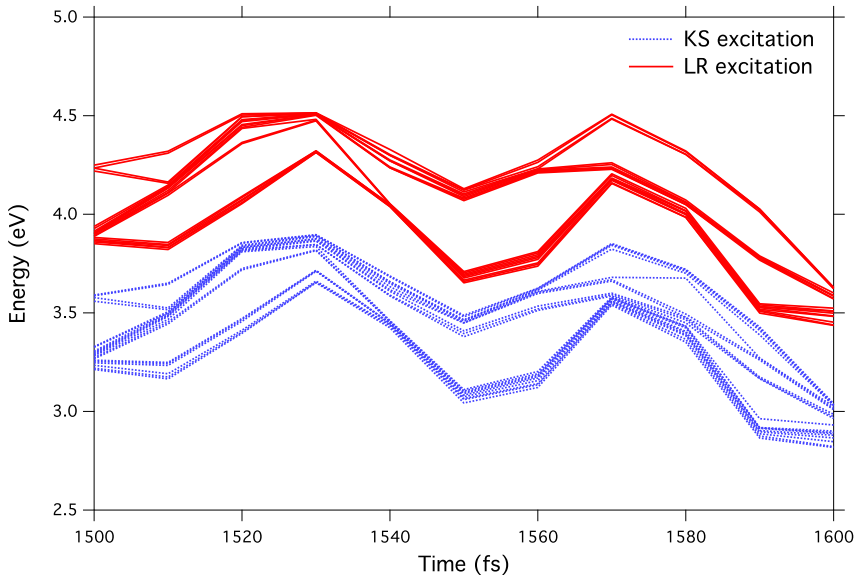

Figure 2.1: The first 19 excited state energies (referenced to the ground state) for a $Si_{29}H_{24}$ quantum dot calculated with LR-TDDFT (red lines) and KS orbital energy differences (blue dashes). The B3LYP exchange-correlation functional was used along with the 6-31G(d,p) basis set for the hydrogens and valence Si electrons, while the LANL2DZ pseudopotential was utilized for the core Si electrons. The energies were calculated with Gaussian [32]

and via taking KS orbital energy differences. While there are differences between the two approaches, overall there is good agreement. The KS excitations are after all the starting point for the LR-TDDFT calculation. It has also been shown that KS excitations are very good approximations to true excitation energies when the true KS potential is used; [76] therefore, as approximate exchange-correlation functionals are improved, the KS excitation energies should improve as well.

It should be noted here that although the formalism described above is applicable to HF theory as well as DFT, the single determinant framework for excited states is expected to generally give better results for DFT rather than HF. This is a consequence of the different ways in which the virtual MOs are evaluated in the two theories. [24] In HF the virtual MO energies are calculated as if there were $N + 1$

electrons in the system, where N is the actual number of electrons. In KS theory the virtual MO energies are still representative of an N-electron system.

Besides the excited state energies and forces, the other major component that governs the dynamics is the non-adiabatic coupling. When single determinants are used to represent the electronic states, the coupling is only going to be non-zero if the determinants differ in a single MO. Therefore, we may underestimate some of the dynamics with this approximation for the wave functions. We showed previously through a semi-classical analysis of transition probabilities that the KS and LR-TDDFT approaches were in good agreement for the Si quantum dot model. [28]. This is backed up by a recent study that showed non-adiabatic couplings calculated from Slater determinant wave functions will be in good agreement with the LR-TDDFT values anytime that the orbital energy difference is a good approximation to the excitation energy. [42] Overall, our method may not accurately capture low probability dynamics and minor reaction pathways, but we should still account for the major reaction channels.

2.3 Computational savings through the classical path approximation

For the calculations discussed below, we made one additional cost saving approximation: the classical path approximation (CPA). Normally with FSSH, the nuclear degrees of freedom are affected by the electronic degrees of freedom through state switches (which change the force on the nuclei) and the accompanying momentum rescaling. Under the CPA, changes in the electronic subsystem do not affect the nuclear evolution, i.e. the nuclear trajectory is pre-determined. This approximation will be valid if electronic states differ little from each other, as is often the case with large systems, or if the energy of the nuclei is sufficiently greater than that of the electrons.

Enormous computational savings can be reaped through the CPA. Because of the stochastic nature of FSSH, hundreds if not thousands of trajectories need to be averaged together per initial condition to obtain meaningful results. Even performing calculations in a single determinant framework, that many unique trajectories would

be computationally prohibitive. By invoking the CPA a single nuclear trajectory can be pre-computed. This trajectory is then used to sample the electronic dynamics.

In order to account for the hop rejection that can occur in the full FSSH procedure, we scale the hopping probabilities by a Boltzmann factor,

$$\beta_{ij} = \begin{cases} \exp\left(-\frac{H_{jj}-H_{ii}}{k_B T}\right), & H_{jj} > H_{ii} \\ 1, & H_{jj} \leq H_{ii} \end{cases} . \tag{2.7}$$

This also ensures we head toward a realistic equilibrium population. With the CPA we can also avoid having to calculate the non-adiabatic coupling vector, and instead we can calculate the non-adiabatic coupling matrix elements via a finite difference approach.

$$\begin{aligned} \dot{\mathbf{R}} \cdot \mathbf{d}_{jk}(\mathbf{R}) &= \left\langle \Phi_j(\mathbf{r};\mathbf{R}) \left| \frac{\partial}{\partial t} \Phi_k(\mathbf{r};\mathbf{R}) \right. \right\rangle_{\mathbf{r}} \\ &\approx \frac{1}{2\Delta t} \left[\langle \phi_q(\mathbf{r};\mathbf{R})_t \left| \phi_s(\mathbf{r};\mathbf{R})_{t+\Delta t} \right\rangle_{\mathbf{r}} \delta_{ab} - \langle \phi_a(\mathbf{r};\mathbf{R})_{t+\Delta t} \left| \phi_b(\mathbf{r};\mathbf{R})_t \right\rangle_{\mathbf{r}} \delta_{qs} \right] . \end{aligned} \tag{2.8}$$

The time subscripts in the above equation refer to the fact that the wave functions depend implicitly on time through their parametric dependence on the nuclear coordinates, and they indicate that the overlap is computed with wave functions from neighboring time steps. The Prezhdo group has made extensive use of the CPA in FSSH simulations and has found very good agreement between their simulations and experimental results. [49, 50, 38, 37, 25, 27] We have included in the appendix the Fortran source code for our program that computes the excitation energies, oscillator strengths, and non-adiabatic couplings, as well as our FSSH program.

Chapter 3

CHARGE TRANSFER STATE FORMATION IN A MN-DOPED ZNO QUANTUM DOT

As a first test of our new implementation of FSSH, we examined the formation of a metal-to-ligand charge transfer ($ML_{CB}CT$) state in a Mn-doped ZnO quantum dot (QD). Understanding the dynamics of the formation of this state, as well as the lifetime, is crucial for future applications involving these magnetically-doped materials.

3.1 Motivation and set-up

Charge carrier dynamics in semiconductor nanocrystals, or QDs, are of interest for their application in biomedical detection, [89, 54] biochemical imaging, [16, 44, 13, 94, 22] solar energy conversion [35, 56, 53, 48] and photocatalysis, [17, 18] and for use in light emitting diodes. [35, 14, 90, 20, 77] Semiconductor QDs posses a unique band structure that spans the gap between bulk materials and molecules. For example, the onset of absorption/emission can be continuously changed by modifying the size of the QD. [1, 36]

Beyond the ability to control electronic excitations by varying the QD's diameter, the incorporation of transition-metal dopants such as Co^{2+} and Mn^{2+} to form diluted magnetic semiconductors (DMSs) introduce new levels which enhance the richness of the absorption spectra. [7, 46, 45] Our group's previous theoretical studies have focused on elucidating the distribution of electronic states and on characterizing the electronic transitions in Mn^{2+}–doped ZnO (Mn^{2+}:ZnO) QDs. [5, 26, 3] However, no comment was made on the relaxation time or pathways for the recombination of the conduction-band (CB) electron (e^-_{CB}) and valence-band (VB) hole (h^+_{VB}). Al-

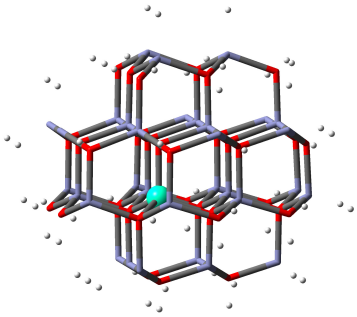

Figure 3.1: Structure of the Mn-doped ZnO QD. The Mn atom is represented by the green sphere, the Zn atoms are represented by the blue segments, the O atoms are represent by the red segments, and the pseudo-H atoms are give by the white spheres.

though studies have examined the dynamics of charge carrier relaxation in pure ZnO nanowires/films [47, 96, 74] and QDs, [15] no known studies have examined the process in Mn^{2+}:ZnO QDs.

The unique electronic structure of Mn^{2+}:ZnO gives rise to new spectral features resulting from the appearance of mid-gap Mn^{2+} $3d$ levels, which have been well characterized both experimentally [69, 51] and theoretically. [26, 3] These new levels give rise to photoionization excited states such as the $ML_{CB}CT$ state described by Eq. 3.1.

$$Mn^{2+} \xrightarrow{h\nu} Mn^{3+} + e^{-}_{CB} \tag{3.1}$$

We recently reported on the observation of spin-dependent hole delocalization among multiple dopant ions in Mn^{2+}:ZnO QDs upon excitation to this $ML_{CB}CT$ excited state which favored parallel Mn^{2+} spin alignment.[26] Crucial to the application of materials that exhibit this form of photomagnetization is a characterization of the dynamics and longevity of the charge carriers responsible for the formation of the $ML_{CB}CT$ excited state. To address this we used the surface hopping approach outlined previously to study the formation of the $ML_{CB}CT$ state following photoexcitation of the band-to-band transition (see Fig. 3.2).

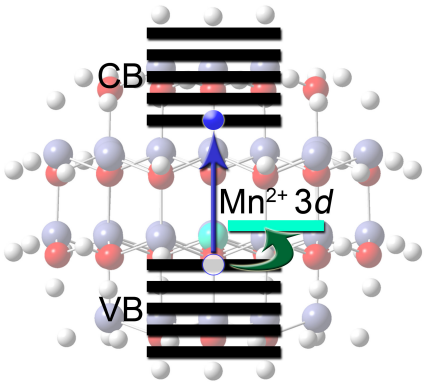

Figure 3.2: Schematic representation of the charge transfer dynamics of interest. After exciting a band-to-band transition in the ZnO QD, a metal-to-ligand charge transfer occurs whereby the hole relaxes into the Mn^{2+} $3d$ levels, creating a Mn^{3+} species.

BOMD was used to determine the nuclear trajectory, from which we extracted energies and non-adiabatic couplings to feed the electronic equation of motion. The BOMD trajectory was computed using the development version of the Gaussian package. [30] The PBE1PBE functional along with the LANL2DZ basis set and effective core potentials were employed for the calculations. Our model QD consisted of an approximately spherical $Zn_{32}MnO_{33}$ cluster (diam. $\sim$1.4 nm) with a wurtzite lattice structure (Fig. 3.1). Pseudo-hydrogen atoms were used to passivate surface valences. [4] Additionally, the mass of each pseudo-hydrogen atom was increased to the mass of Zn or O, depending on the pseudo-hydrogen location, in order to avoid unphysical, high-frequency vibrations.

The geometry of the QD was first optimized at 0 K. Then the structure was brought up to 300 K via repeated velocity rescaling with 10 steps of energy-conserving dynamics between each velocity adjustment. A 1 ps BOMD trajectory with a 1 fs time step was then computed. The density matrix version of Eq. 2.3 was integrated along the pre-computed nuclear trajectory using a fourth-order Runge-Kutta scheme with a 10^{-3} fs time step. Electronic energies and non-adiabatic couplings were linearly interpolated between nuclear time steps. The initial electronic state for each run of the surface hopping dynamics was chosen based on the state with the highest oscillator strength within the energy window 6.2-6.5 eV. This energy corresponds to the main excitonic peak in the calculated absorption spectrum, while the energy spread corresponds to the experimental broadening of the absorption spectrum. Oscillator strengths were calculated via the following:

$$f_{aq} = \frac{2m_e \left(\epsilon_q - \epsilon_a\right) \mu_{qa}^2}{3\hbar^2}, \tag{3.2}$$

where MO a was replaced by MO q in the ground state determinant and μ_{qa} is the MO dipole matrix element for MOs a and q, $\mu_{qa} = \langle \phi_q \left| \hat{\mu} \right| \phi_a \rangle$, with $\hat{\mu}$ being the dipole moment operator. Two hundred different initial conditions were sampled with 10,000 surface hopping trajectories of 800 fs launched for each initial condition, making the final population results averaged over 2 million trajectories.

3.2 Relaxation dynamics

Displayed in Fig. 3.3 are representations of the highest occupied molecular orbital (HOMO) and lowest unoccupied molecular orbital (LUMO). The HOMO has significant localization around the Mn atom, while the LUMO is delocalized across the core of the QD. In the equilibrium geometry, the five lowest excited state are all $\mathrm{ML_{CB}CT}$ states, with the lowest three sitting inside the band gap of ZnO. At 300 K though, the higher two $\mathrm{ML_{CB}CT}$ states mix significantly with the ZnO excitonic transitions. The lowest three excited states remain mostly separated from the rest of the excited states

due to their location inside the normal ZnO band gap (see Fig. 3.4) and maintain their $ML_{CB}CT$ character.

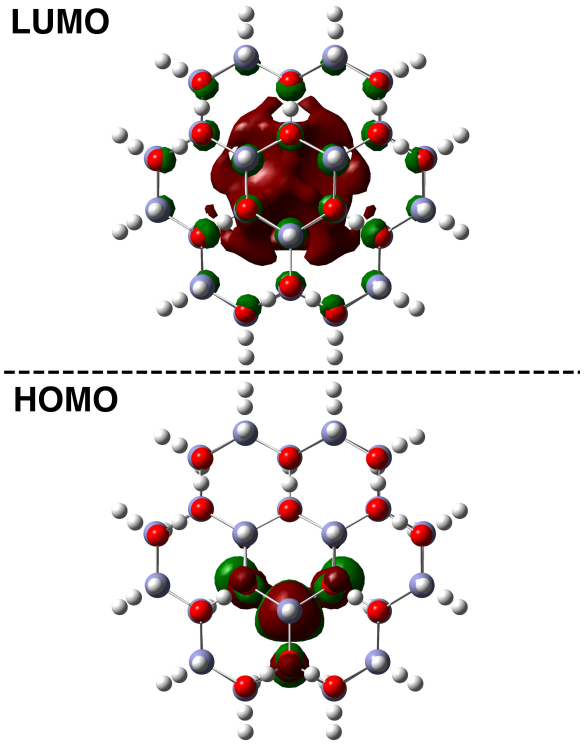

Figure 3.3: Isosurface plots of the HOMO and LUMO of our Mn^{2+}ZnO QD in the optimized ground state geometry. The HOMO shows significant localization around the Mn atom, while the LUMO is delocalized across the QD core.

Shown in Fig. 3.5 is the calculated absorption spectrum. We have plotted both the oscillator strengths that we calculated (see Eq. 3.2) and the curve resulting from fitting Gaussian functions to each transition. We calculated the oscillator strengths for the first 99 transitions at each of the first 200 nuclear configurations of our BOMD trajectory, making our spectrum representative of an ensemble of QDs. Our absorption spectrum is in excellent agreement with experimental absorption spectra for Mn-doped ZnO. [6]. The Mn-dopant creates a broad shoulder at the onset of absorption, while we also observe the small dip in absorption following the first excitonic

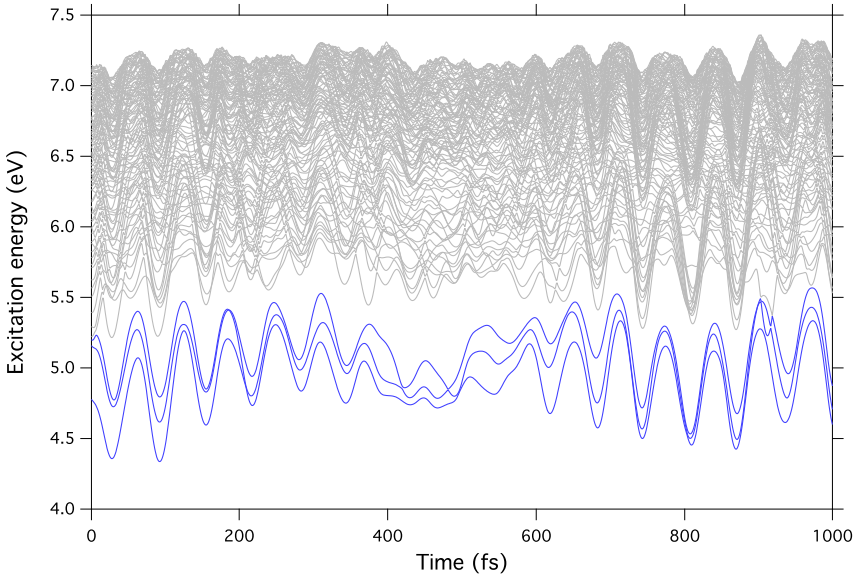

Figure 3.4: Excitation energies as a function of time for the first 99 excited states. The $ML_{CB}CT$ states are marked in blue.

peak, which is more pronounced in smaller QDs. [93] This excellent agreement is a sign that our single determinant framework is a good approximation for this system.

Our main result is shown in Fig. 3.6, where we have plotted the ground state and $ML_{CB}CT$ state populations as a function of time. The rise in the population of the $ML_{CB}CT$ state occurs on an ultrafast time scale (see inset of Fig. 3.6). Within approximately 20 fs, the $ML_{CB}CT$ state is almost fully populated: a good sign for the prospect of photoinduced magnetization. Unfortunately, the state appears to have a relatively short lifetime ($\sim$500 fs). The typical time scale for magnetic polaron formation is 100s of ps. [23] So it would appear that the $ML_{CB}CT$ state does not live long enough at room temperature in order to align the spins of the dopants.

At lower temperatures though, the lifetime of the $ML_{CB}CT$ state is significantly extended. As an example of this, we have the relaxation dynamics for the same system at 1 K. While this is not a physically realistic temperature for the system, it does illustrate a point about the dynamics. When the QD is cooled down, the dynamics

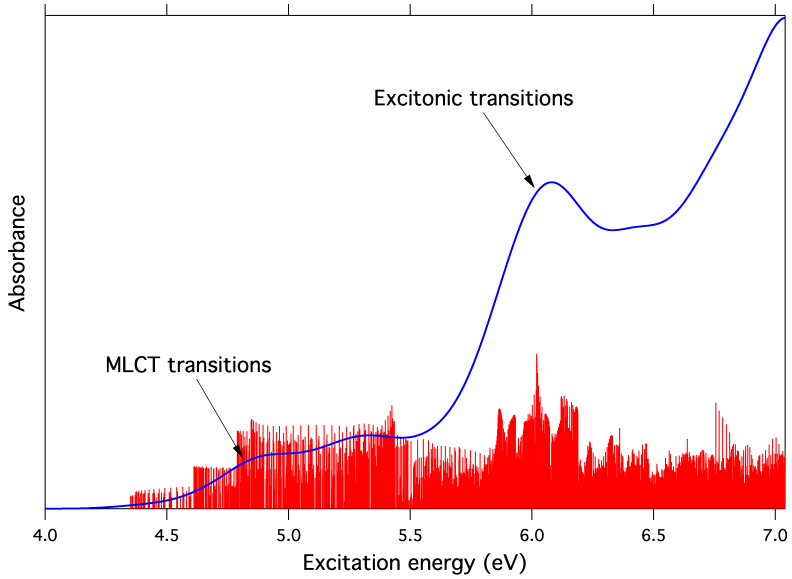

Figure 3.5: Calculated absorption spectrum for our QD. The red sticks are the calculated oscillator strengths for the first 99 excited states over the first 200 time steps of the BOMD trajectory. The blue line was computed by fitting a Gaussian function to each stick and summing the contributions at every energy. We used a width of 0.16 eV, which corresponds to the experimental broadening of the absorption spectrum. The blue line has been scaled down in order to fit on the same plot as the oscillator strengths.

are substantially slowed down. The formation of the $ML_{CB}CT$ state now occurs with a time constant around 1 ps, while its non-radiative lifetime is estimated to be on the order of a nanosecond. This dramatic slowing of the dynamics is caused by two factors, which can be seen in Eq. 1.11. First, the lower temperature means slower nuclei. The nuclear velocity appears as a pre-factor on the non-adiabatic coupling, meaning that slower nuclei induce less exchange between states. Additionally, the non-adiabatic coupling itself is expected to be smaller at lower temperatures for the $ML_{CB}CT$ state. The coupling for the $ML_{CB}CT$ state is related to the overlap of highly localized Mn^{2+} $3d$ MOs with delocalized ZnO MOs. Thermal fluctuations cause the Mn^{2+} $3d$ MOs to delocalize some and thereby increase their overlap with the ZnO MOs. As thermal fluctuations die down with decreased temperature, the Mn^{2+} $3d$

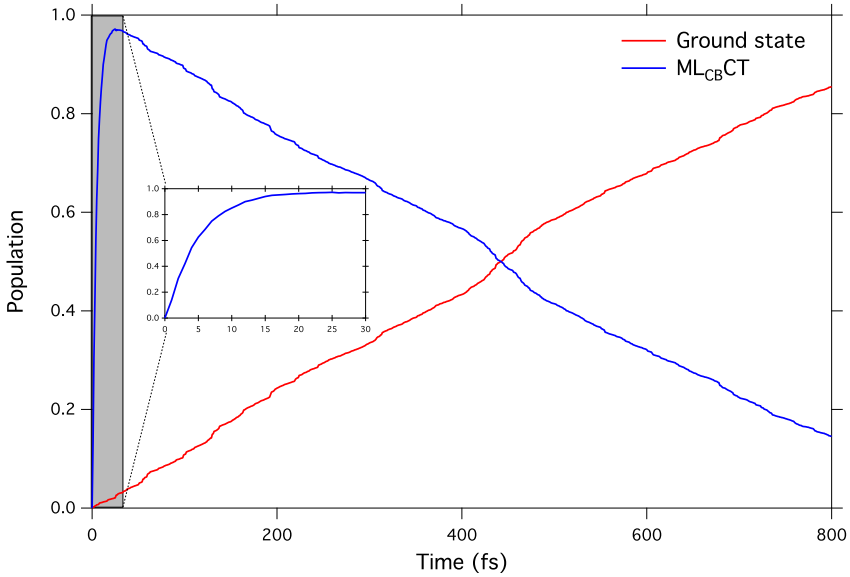

Figure 3.6: Relaxation dynamics of the Mn-doped ZnO QD at 300 K. Displayed are the ground state population (red line) and $ML_{CB}CT$ state population (blue line). The inset shows the early time dynamics of the $ML_{CB}CT$ state.

MOs will stay more localized, decreasing the non-adiabtic coupling to the $ML_{CB}CT$ state.

Based on our dynamical simulations, the formation of an ordered spin state, following excitation of a Mn-doped ZnO QD and relaxation into the $ML_{CB}CT$ state, does not seem likely at room temperature. While the $ML_{CB}CT$ state forms on an ultrafast time scale, its lifetime falls short of reported spin ordering times. The process may be feasible at lower temperatures where the relaxation dynamics are dramatically slowed.

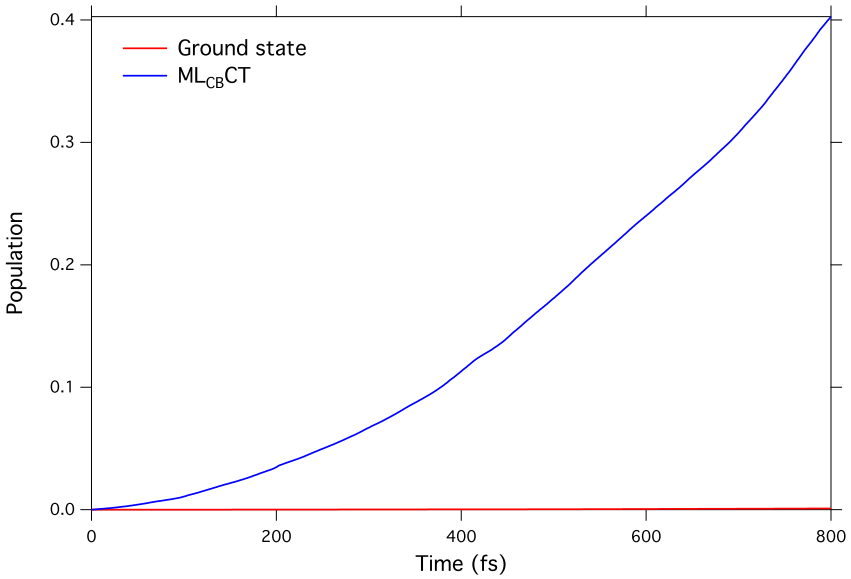

Figure 3.7: Relaxation dynamics of the Mn-doped ZnO QD at 1 K. Displayed are the ground state population (red line) and $ML_{CB}CT$ state population (blue line).

Chapter 4

EXCITON RELAXATION DYNAMICS OF A SERIES OF CONJUGATED COPOLYMERS

The relaxation dynamics of the electron donor phase of organic photovoltaics makes for an interesting second test of our FSSH implementation. There are many open questions concerning exactly how to improve efficiencies in organic photovoltaics. Advances in experimental techniques are beginning to unravel some of these mysteries, but there is a need for more theoretically modeling, specifically dynamical simulations, to help interpret experimental results and offer insights into which directions to explore next.

4.1 Motivation and set-up

Organic solar cells comprise an exciting field where chemistry, physics, and materials science all converge to address a problem that has the potential to impact the entire planet. They hold the promise of a low-cost, light-weight alternative to traditional inorganic solar cells. However, much work is still needed to achieve the stable devices with high efficiencies that are needed to make organic solar cells economically feasible. [81] Perhaps the most promising type of organic solar cell is the bulk heterojunction (BHJ). [39, 97] BHJ solar cells consist of an interpenetrating network of donor and acceptor phases. The most common acceptor phases are derivatives of fullerenes, with [6,6]-phenyl-C_{61}-butyric acid methyl ester ($PC_{61}BM$ or $PC_{71}BM$) proving to be almost ideal. Most research efforts then have focused on the design of conjugated polymers for the electron donor phase.

Based on the electronic structure of PCBM and the solar spectrum, the ideal

electron donor is often considered to have a LUMO level at 3.9 eV and a HOMO level at 5.4 eV, relative to the vacuum level. [81] The LUMO level is chosen to create an offset with the LUMO level of PCBM in order to create a driving force for exciton dissociation. The Coulombic attraction between electron and hole in organic polymers is typically estimated to be 0.4-0.5 eV, [2] so the LUMO offset needs to be such that this attraction can be overcome. At the same time, studies have shown that excess driving force does not improve efficiencies, but rather results in wasted energy. [12, 92] A large electron mobility would also be a pre-requisite for an ideal electron donor.

The use of copolymers greatly enhances the possibilities for tuning donor properties in order to enhance BHJ solar cell efficiencies. One promising approach that was recently put forth is coupling indacenodithiophene (IDT) units to the variations of the electron deficient quinoxaline unit. [99] In particular IDT combined with phenanthrenequinoxaline (phanQ) performed particularly well. A PIDT-phanQ/$PC_{71}BM$ device showed a power conversion efficiency (PCE) of 6.24%. Another study found that the addition of fluorine to a different IDT-based donor increased device performance. Devices containing mono-fluorinated and di-fluorinated polymers gave PCEs of 5.40% and 5.10%, respectively. For reference, the device with the un-fluorinated polymer had a PCE of 5.02% under the same conditions. [98]

The question now is can the same be achieved with the PIDT-phanQ polymer, which already showed a PCE above 6%. Another interesting related question is why the di-fluorinated polymer performed worse than the mono-fluorinated polymer. Our newly implemented FSSH method seems to be well suited to provide some insight into these questions. Shown in Fig. 4.1 are the structures of the monomer units that we chose to study first. Future work will be concerned with alternate placements of the fluorine atoms, as well as moving beyond an isolated monomer unit.

A development version of the Gaussian program was used to perform BOMD calculations in order to obtain our nuclear trajectories along with our electronic energies and non-adiabatic couplings. [31] This time we used the B3LYP exchange-correlation

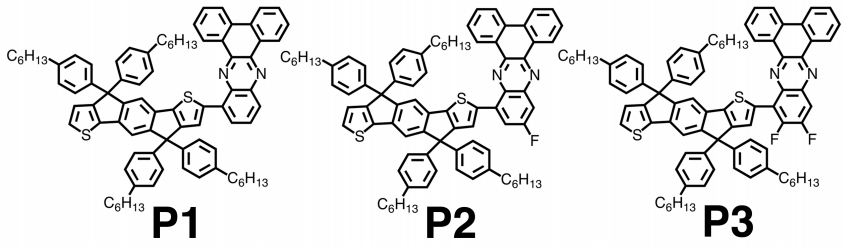

Figure 4.1: Structure of the three monomer units that were studied.

functional and the 6-31G(d) basis set. The geometry of each monomer was first optimized at 0 K before the structures were brought up to 300 K via repeated velocity rescaling with 10 steps of energy-conserving dynamics between each velocity adjustment. BOMD trajectories of 400 fs each with a 0.5 fs time step were then computed. The density matrix version of Eq. 2.3 was integrated along the pre-computed nuclear trajectory using a fourth-order Runge-Kutta scheme with a 10^{-3} fs time step. Electronic energies and non-adiabatic couplings were linearly interpolated between nuclear time steps.

For the first set of dynamics we discuss below, the initial state was simply taken as the first excited state. For the second set of dynamics the initial electronic state was chosen based on the state with the highest oscillator strength within the energy window 3-4.25 eV, which corresponds to the second major peak in the absorption spectra. Oscillator strengths were calculated again calculated according to Eq. 3.2. Two hundred different initial conditions were sampled. We ran 10,000, 300-fs long surface hopping trajectories for each initial condition, making the final population results averaged over 2 million trajectories.

4.2 Relaxation dynamics

Figure 4.2 shows the HOMOs and LUMOs for each of the three monomers. For all three the HOMO is spread across the monomer backbone while the LUMO is localized

on the phanQ units. This HOMO-LUMO arrangement makes the lowest excited state an intra-molecular charge transfer state. Not only does this lower the band gap of the polymer, but the delocalized nature of the excited state is potentially beneficial for fast and efficient charge transfer across the polymer-fullerene interface. The addition of the fluorine atoms to the phanQ units do not significantly alter either the HOMOs or LUMOs.

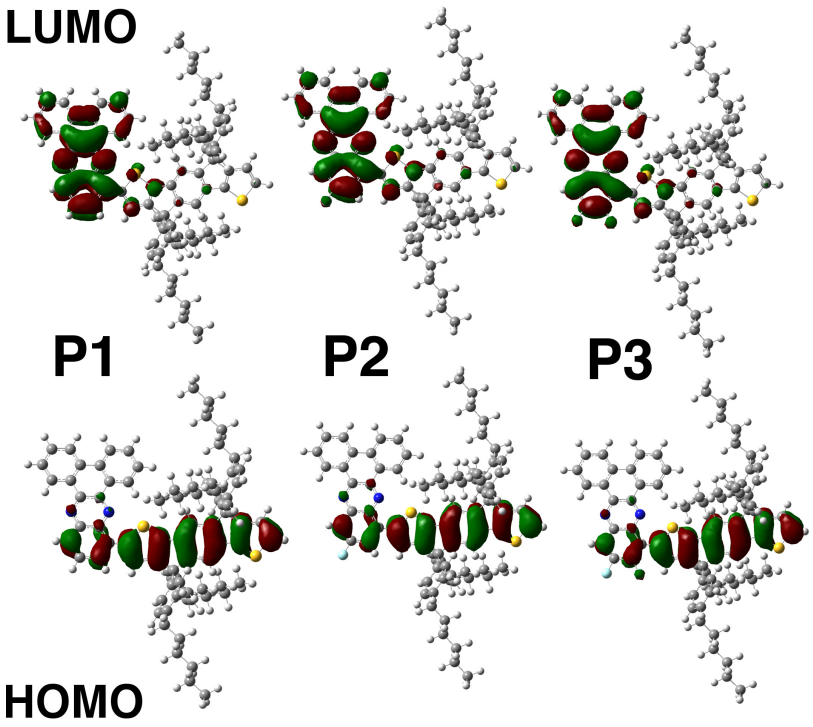

Figure 4.2: HOMOs and LUMOs for the studied monomers. The HOMOs are all localized along the backbone of the monomer while the LUMOs are localized on the phanQ units.

Shown in Fig. 4.3 are excitation energies as a function of BOMD trajectory time for the first 99 excited states of each monomer. Even at the level of a monomer of the polymer, the excited state manifold is very dense. Again the addition of the fluorine atoms does not appear to cause any significant changes. We have highlighted the

lowest excited state as the charge transfer nature of this state makes it well suited for efficient further charge transfer to an acceptor species and it represents the last chance for the exciton to separate before recombination loss back to the ground state. As such our simulation focuses on the dynamics in this state.

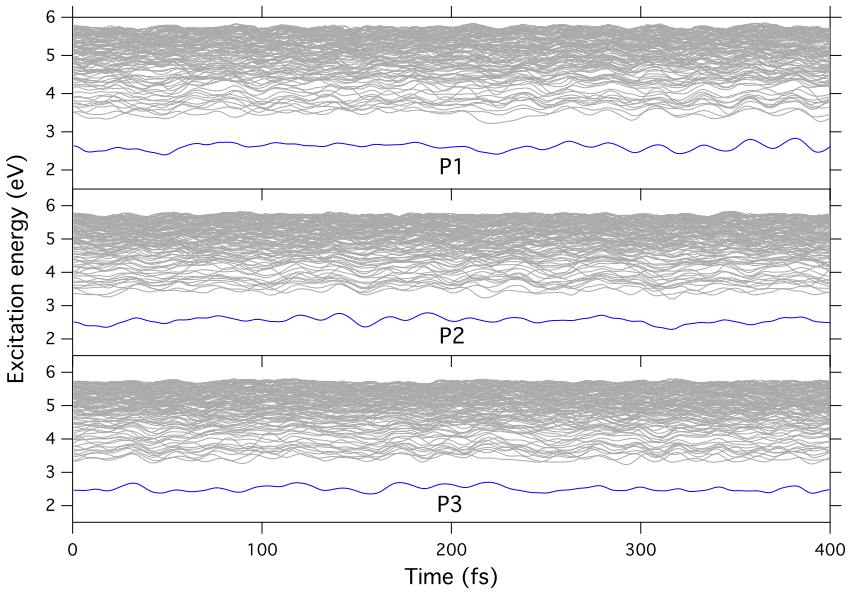

Figure 4.3: Excitation energies over the course of the BOMD trajectories for the three monomers. The lowest excited state is highlighted in blue.

We calculated ensemble averaged absorption spectra for each of the monomers with the results displayed in Fig. 4.4. The absorption spectrum for each monomer is a combination of 200 individual absorption spectra. It is here we can see the effect of the fluorine atoms. The first peak in the absorption spectra corresponds to excitation to the lowest excited state. The position of this peak red-shifts with added fluorine. This is due to fluorine increasing the electron affinity of the phanQ unit, resulting in a lowered LUMO energy. The position of the second peak in the absorption spectra is less affect by the fluorine atoms. Additionally, there is a slight increase in the intensity of absorbance with added fluorine due to the increase in the molecular dipole. The absorption spectrum for the P1 monomer is in good qualitative agreement with

previously published absorption spectra for the corresponding polymer. [99] Again indicating that our dynamics simulation should provide some reliable insight.

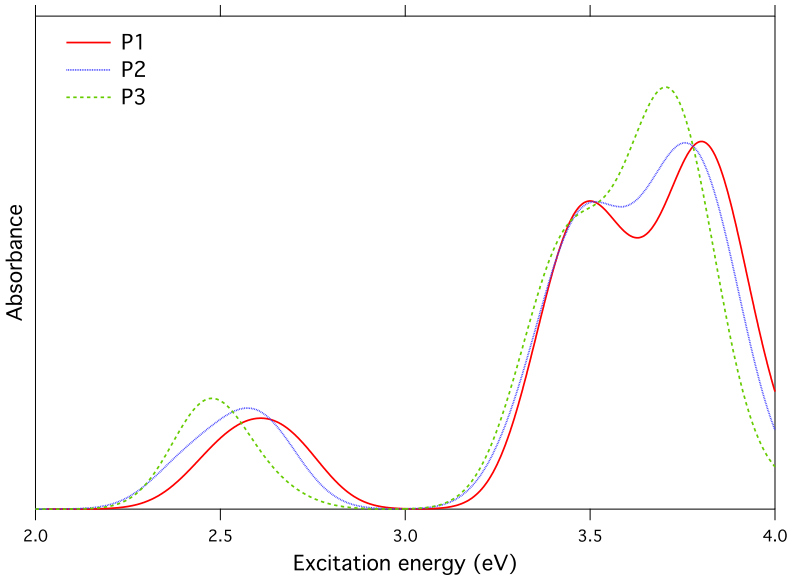

Figure 4.4: Calculated absorption spectra for our three monomers. The lines were calculated in the same manner as before for the ZnO QD: a Gaussian function of width 0.13 eV (estimated broadening from the experimental spectrum for P1) was fit to each calculated oscillator strength (not shown), and the contributions were summed at every energy. Absorption spectra from 200 different nuclear configurations were sampled for each line. Monomer P1 is given by the solid, red line, P2 is the dotted, blue line, and P3 is the dashed, green line.

Our first dynamical simulation began with the first excited state being occupied. Figure 4.5 shows the relaxation dynamics of the first excited state population. All three monomers relax very fast with all relaxations complete by approximately 200 fs. The fluorine atoms appear to have the effect of enhancing relaxation to the ground state. The P3 monomer with two fluorine atoms relaxes the fastest, and the P1 monomer without any fluorines has the slowest relaxation.

Recently studies have suggested that the formation of hot charge transfer states (i.e. transferring the electron to the fullerene before the exciton relaxes on the poly-

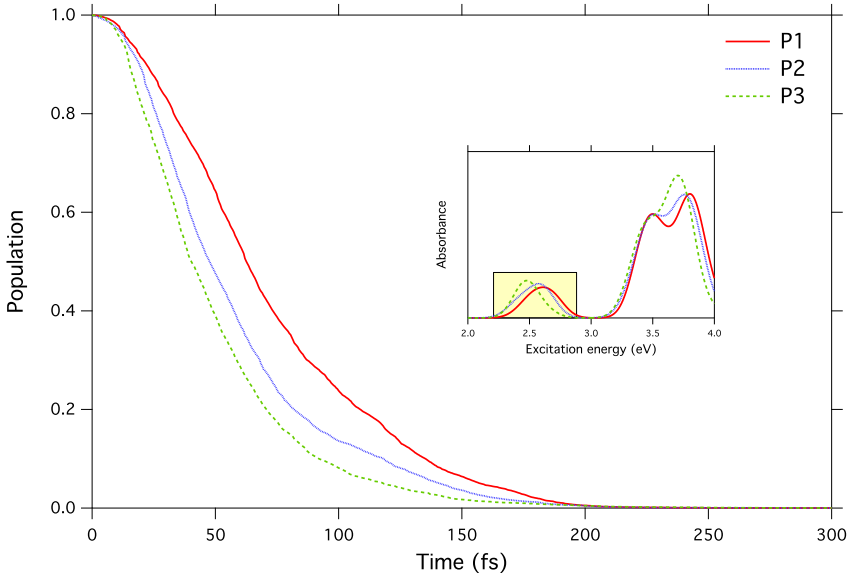

Figure 4.5: Relaxation dynamics for our three monomers. The starting electronic state was the first excited state (highlighted region on the inset absorption spectra), and displayed is the population of that state. Monomer P1 is given by the solid, red line, P2 is the dotted, blue line, and P3 is the dashed, green line.

mer) are important for high efficiency in polymer solar cells. [34, 43] To examine the feasibility of forming hot charge transfer states with these polymers, we performed a second set of calculations where our initial electron state came from the second peak in the absorption spectra. These results are shown in Fig. 4.6 where again we have plotted the population dynamics of the first excited state. Relaxation into the first excited state occurs on an ultrafast time scale; all three monomers complete relaxation to the first excited state within the first 20 fs of the simulation. Subsequent relaxation to the ground state occurs very similar to what was seen when we began the simulation in the first excited state.

Interestingly, the relaxation into the first excited state does not follow the same trend that was seen for relaxation into the ground state. The monomer with a single fluorine atom shows faster relaxation to the first excited state, followed by monomer P3 then P1. Relaxation to ground state then proceeds in the same order as the

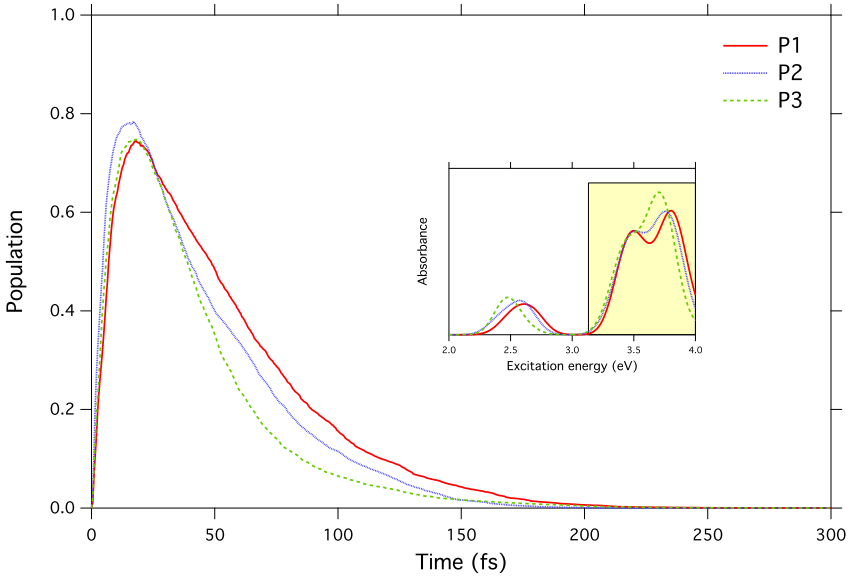

Figure 4.6: First excited state population as a function of time for the three monomers. The starting electronic state here was the state with the high oscillator strength under the second peak in the absorption spectra (highlighted region on the inset absorption spectra). Monomer P1 is given by the solid, red line, P2 is the dotted, blue line, and P3 is the dashed, green line.

previous calculation with P3 relaxing the fastest even though P2 made it to the first excited state first. The P2 monomer also achieves a slightly larger population of the first excited state before beginning relaxation to the ground state.

The relaxation to the ground state is inversely proportional to the band gap of the monomer (e.g. P1 has the largest band gap and the slowest relaxation); however, the relaxation does not correlate perfectly with the average magnitude of the non-adiabatic coupling between the first excited state and the ground state. In Fig. 4.7 we have plotted a running average of the magnitude of the coupling between the first excited state and the ground state. For each initial condition we averaged the magnitude of the non-adiabatic coupling over the first 100 fs of the trajectory that began at that initial condition. For the first 80 initial conditions, monomer P2 shows the largest average coupling. For the remaining initial conditions, monomer P3 has

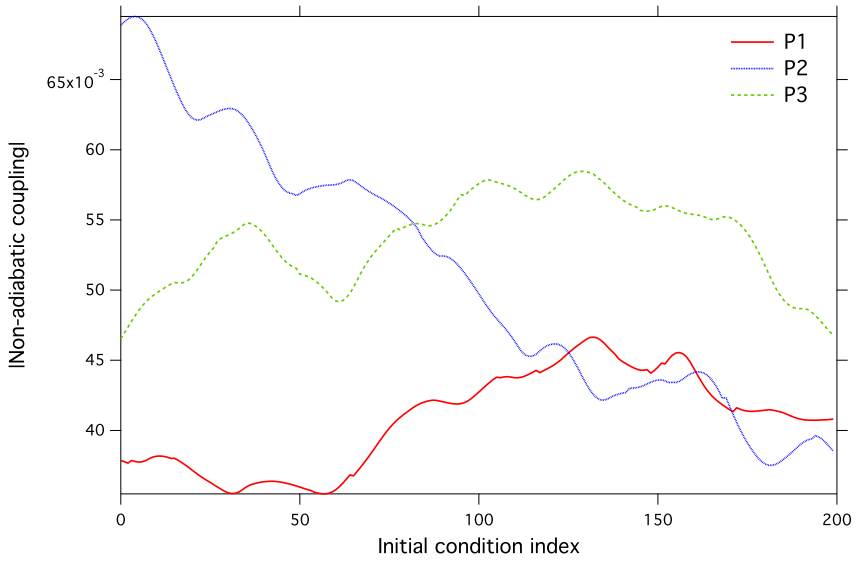

Figure 4.7: Average magnitude of the non-adiabatic coupling between the first excited state and the ground state over the first 100 fs of the trajectories beginning from each initial condition.

the largest average coupling, while P2 and P1 have approximately the same coupling.

Of course the non-adiabatic coupling is not the only factor determining the relaxation. The hopping probability also depends on the off-diagonal density matrix element between the states in question. Additionally, since the hopping probability is proportional to the product of non-adiabatic coupling and off-diagonal density matrix element, there has to be a sort of resonance between the two in order to promote transitions. The hopping probability will be zero if either the non-adiabatic coupling or the off-diagonal density matrix element is zero, or if they are of the same sign (see Eqs. 1.14 and 1.13). The P3 monomer appears to best meet this condition. We examined the average dynamics over just the first 50 initial conditions, where P2 has higher average coupling than P3, and found the two monomers to show the same relaxation time.

The addition of fluorines to the monomers has a two-fold effect on the system. The fluorines lead to an enhancement of the absorbance of the monomer as the fluorines

enhance the dipole moment of the monomer. This is advantageous from a solar cell perspective as a high absorbance means more excitons that could potentially be separated. The other effect is not as advantageous for solar cells; the fluorines appear to speed up exciton relaxation.

Ideally, excitons would be separated and charge carriers extracted before any thermal relaxation can occur. If the relaxation becomes too fast, then recombination to the ground state will occur before there is a chance for charge transfer to the electron acceptor. A recent study on another low band gap polymer/PCBM system found the time scales for charge transfer from the polymer to the fullerene to be around 50 fs. [34] That is close to the time scale for relaxation seen for the fluorinated monomers, and so there may be a competition between charge transfer and recombination to the ground state, especially for the doubly fluorinated monomer.

Chapter 5

SURFACE HOPPING WITH EHRENFEST EXCITED POTENTIAL

Motivated by the electronic structure of systems like the previous examples, we have developed a modification of the FSSH method that takes advantage of the difference in the energy spacing between the ground and excited states versus the energy spacing between excited states. Termed surface hopping with Ehrenfest excited potential (SHEEP), our method simplifies the representation of the excited states with an Ehrenfest-like treatment while still utilizing a FSSH-like approach for determining the population dynamics. The greatest draw of SHEEP is that it can be formulated without any explicit reference to excited state wave functions.

5.1 SHEEP theory

The central idea behind SHEEP is to simplify FSSH via modifying the treatment of the quantum back reaction, i.e. the effect changes in electronic state populations have on the nuclear dynamics. Ehrenfest dynamics simplifies the quantum back reaction via the use of a single PES for propagation; however, this approach is unable to properly account for different reaction pathways and does not approach a realistic equilibrium, expect in the high temperature limit. A common feature of the systems in which we are often interested is a dense manifold of excited states along with a substantial gap between the ground state and the excited states.

Averaging together all of the electronic states in such a system would seem not to be ideal given the energetic gap between the ground state and the excited states. On the other hand, explicitly accounting for all of those states and their interactions, as

would be the case for FSSH, is a computationally daunting task without a handful of approximations. Our solution is to combine these two approaches: treat the excited states with an Ehrenfest-like approach while maintaining a distinct ground state and making surface hops between the ground state and excited state manifold. This is illustrated in Fig. 5.1.

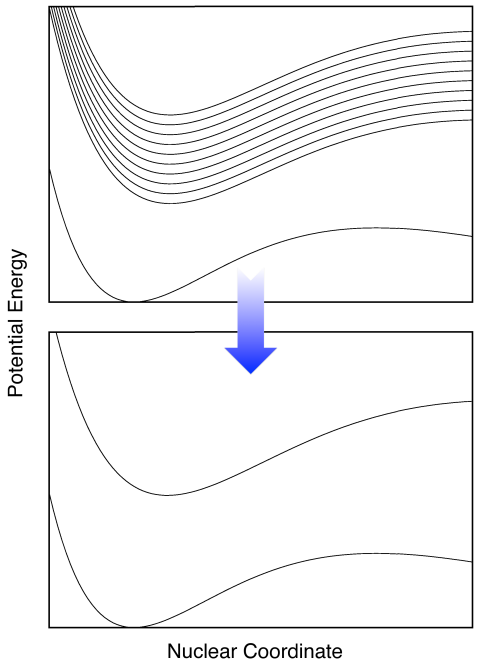

Figure 5.1: Schematic representation of SHEEP. The ground state remains unaltered while all of the excited states are folded into a single, average excited state.

In essence we create a two-state system for the nuclear subsystem, while still treating the electronic subsystem with the time-dependent electronic Schrödinger equation (Eq. 1.11). This is accomplished by transforming the normal electronic basis into a new basis anytime we need to modify the dynamics of the nuclear subsystem (e.g.

applying forces or testing for a transition). Our new basis is given by

$$\Upsilon_G(\mathbf{r};\mathbf{R}) = \Phi_0(\mathbf{r};\mathbf{R}) \tag{5.1}$$

$$\Upsilon_E(\mathbf{r},t;\mathbf{R}) = \sum_{k>0} c_k(t)\Phi_k(\mathbf{r};\mathbf{R}). \tag{5.2}$$

The first state is simply the adiabatic ground state, while the second is our mean-field excited state, being a linear combination of the remaining adiabatic states. The forces on the nuclei are now given by

$$M\ddot{\mathbf{R}} = -\nabla_{\mathbf{R}}\left[\frac{\langle\Upsilon_k|\hat{\mathcal{H}}_{el}|\Upsilon_k\rangle_{\mathbf{r}}}{\langle\Upsilon_k|\Upsilon_k\rangle_{\mathbf{r}}}\right]. \tag{5.3}$$

The normalization is needed for the new excited state. Evaluating the force expression for the mean-field excited state directly would involve excited state energies and couplings, which we would prefer to avoid having to calculate. We can accomplish this in one way by computing the mean-field excited state force through a finite difference of the mean-field excited state energy, which we can define in terms of the full mean-field energy and the ground state energy:

$$\begin{aligned}\langle\Upsilon_E(\mathbf{r},t;\mathbf{R})|\hat{\mathcal{H}}_{el}(\mathbf{r},\mathbf{R})|\Upsilon_E(\mathbf{r},t;\mathbf{R})\rangle_{\mathbf{r}} &= \langle\Omega(\mathbf{r},t;\mathbf{R})|\hat{\mathcal{H}}_{el}(\mathbf{r},\mathbf{R})|\Omega(\mathbf{r},t;\mathbf{R})\rangle_{\mathbf{r}} \\ &\quad - a_{GG}(t)\langle\Upsilon_G(\mathbf{r};\mathbf{R})|\hat{\mathcal{H}}_{el}(\mathbf{r},\mathbf{R})|\Upsilon_G(\mathbf{r};\mathbf{R})\rangle_{\mathbf{r}}.\end{aligned} \tag{5.4}$$

While a finite difference scheme for the force is not ideal, it will be generally preferable to having to calculate all of the excited state energies and couplings. The full mean-field state can be obtained without explicit excited states through propagation of a superposition state. [55]

Hopping probabilities are now also calculated without reference to excited state quantities:

$$g_{GE} = \frac{-\Delta t\dot{a}_{GG}(t)}{a_{GG}(t)} \tag{5.5}$$

$$g_{EG} = \frac{\Delta t\dot{a}_{GG}(t)}{1-a_{GG}(t)}, \tag{5.6}$$

where $a_{GG} = a_{00}$. This definition of hopping probabilities is consistent with the original FSSH algorithm for the case of only two states (see Eqs. 1.12 - 1.14). Having defined the new forces and hopping probabilities we can now outline the method.

Step 1. The initial positions and momenta of all the atoms, along with the initial density matrix, are specified.

Step 2. The classical equations of motion (Eq. 5.3) are integrated a small time step Δt on the PES of the currently occupied electronic state. Equation 1.11 is integrated along this trajectory. Equivalently, Eq. 1.5 could be integrated along this trajectory, and then the ground state projected onto the total wave function to determine the ground state density matrix element after integration.

Step 3. The hopping probability from the current state to the other state is computed according to Eq. 5.5 or 5.6. A random number on the interval (0,1) is generated and compared to the hopping probability. If the hopping probability is greater than the random number, then a switch to the other state is invoked. If the hopping probability is less than the random number, then no transition occurs.

Step 4. If no transition was called for, then return to step 2. If a switch to the other state is called for, the component of the momentum in the direction of the non-adiabatic coupling vector is adjusted so as to conserve energy. If there is insufficient kinetic energy to accommodate the change in potential energy, then the state switch is aborted and the trajectory continues unaltered on the original PES. This is opposed to the original formulation of the fewest switches algorithm where, if a hop was rejected, the velocity along the non-adiabatic coupling vector changed sign. [82, 40] A study by Müller and Stock indicated that better accuracy could be obtained by leaving the velocity unchanged if a hop is rejected. [68] After evaluating the hop, return to step 2.

Not requiring excited state wave functions represents a large computational advantage for SHEEP. We no longer, necessarily, have to choose between accuracy and efficiency for non-adiabatic dynamics calculations on large systems. Previous imple-

mentations of surface hopping have called for either highly-correlated, wave function based methods [88] for an accurate treatment of excited states at the cost of being limited to small molecules, or sacrificing some accuracy in the description of the excited states while gaining the ability to treat larger system by implementing within the Kohn-Sham [21] or linear-response [80] formalisms of time-dependent density functional theory. With SHEEP the total electronic wave function can be represented as a superposition state [55] and the ground state coefficient obtained through projection of the ground state onto the superposition state.

5.2 Model problems

SHEEP can be considered an approximation to FSSH when there are more than two adiabatic states (the methods are the same when there are only two adiabats). As such we explored model problems with a few adiabatic states to ones with many, and compare our results to those of FSSH, as well as Ehrenfest, or mean-field (MF), dynamics. [29] Our first model problem consists of three electronic states with multiple avoided crossings.

The matrix elements of the electronic Hamiltonian in the diabatic representation and atomic units are

$$H_{11}(R) = 0.0 \tag{5.7a}$$

$$H_{22}(R) = 0.045 \tag{5.7b}$$

$$H_{33}(R) = -0.10\exp(-0.28R^2) + 0.05 \tag{5.7c}$$

$$H_{12}(R) = H_{21}(R) = 0.0 \tag{5.7d}$$

$$H_{13}(R) = H_{31}(R) = 0.015\exp(-0.06R^2) \tag{5.7e}$$

$$H_{23}(R) = H_{32}(R) = 0.035\exp(-0.06R^2) \tag{5.7f}$$

The adiabatic potential energy curves for the model studied here are presented in Fig. 5.2, along with the various non-adiabatic couplings for the system. The model

is an extension of Tully's second model problem [82], retaining the dual avoided crossing that produces quantum interference effects in the excitation probabilities while introducing a third state to test the sensitivity of the results with respect to the exact nature of the forces on the nuclear coordinate.

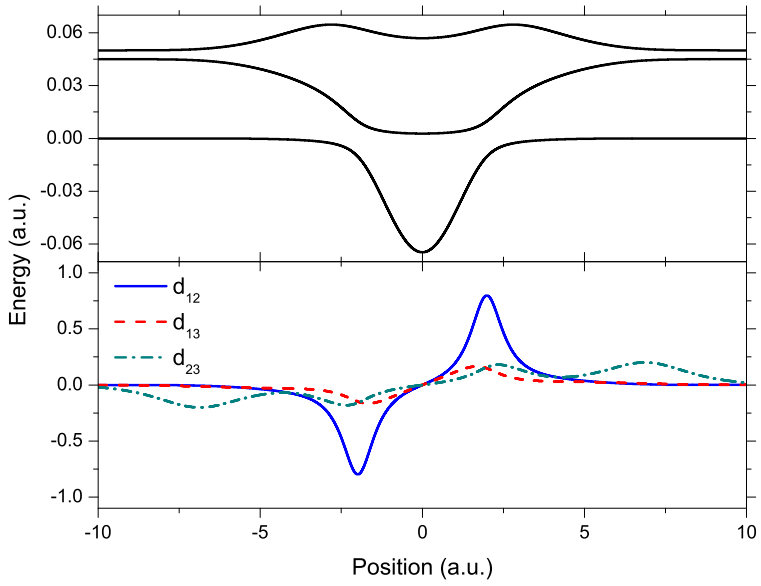

Figure 5.2: Three states with multiple avoided crossings model. Top panel: Adiabatic potential energy curves as a function of the nuclear coordinate. Bottom panel: Non-adiabatic coupling strengths between adiabatic states as a function of the nuclear coordinate.

The classical particle, of mass 2000 a.u., starts each trajectory in the asymptotic negative R region on the ground electronic state with momentum k along the direction of positive R. Each trajectory was integrated until the particle had completely left the interaction region. For the SHEEP and FSSH results, 2000 trajectories were run for each value of initial momentum, ranging from $k = 5$ a.u. to $k = 40$ a.u. The final probabilities for both the SHEEP and FSSH methods were computed in the usual way by simply considering the fraction of trajectories that achieved each outcome.

For the MF method, the value of the appropriate density matrix element along the diagonal at the time the integration was stopped is given as the final probability.

Shown in Fig. 5.3 are the various probabilities for transmission on the ground state (Fig. 5.3a), reflection on the ground state (Fig. 5.3b), and transmission on either excited state (Fig. 5.3c), all as a function of initial momentum. There is no reflection on any excited state. The SHEEP and FSSH results are in near perfect agreement over the entire momentum range considered. The MF method is only capable of giving either reflection or transmission for a given initial momentum. The potentials in this model are such that reflection is never seen from the MF method. This result is the reason for maintaining at least two states for nuclear dynamics in SHEEP.

To demonstrate that SHEEP can provide meaningful information about the populations of the individual excited states, Fig. 5.4 shows the probabilities for transmission on the individual excited states. Again the SHEEP and FSSH results are in near perfect agreement over the entire energy range. We do concede though that since the excited state in SHEEP is treated in a mean-field manner, higher-lying excited states could see some unphysical population much in the same way that MF dynamics will populate states that are not energetically accessible. However, we feel that this should be mediated somewhat by the energy conservation criteria of the surface hopping. If a highly-excited basis state is predicted to have significant population, it will contribute more to the energy of the mean-field excited state in SHEEP. This added contribution will raise the energy of the mean-field excited state, forcing the system to need more energy in order to transition out of the ground state.

The results of all three methods converge at higher momenta, which is to be expected since with increasing momentum, the amount of time the particle spends in the interaction region is accordingly decreased and will therefore be less sensitive to the exact manner in which it traverses that region. The results at lower momentum illustrate some advantages surface hopping based methods possess over the MF approach.

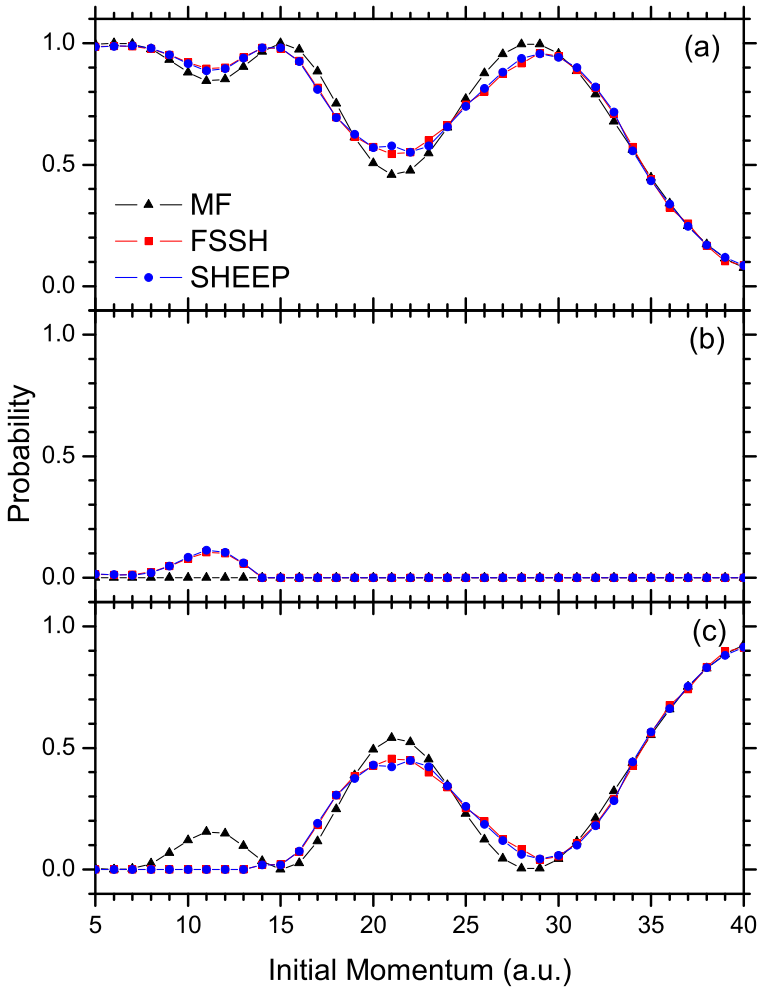

Figure 5.3: Three states with multiple avoided crossings model. (a) Probability of transmission on the ground adiabatic state. (b) Probability of reflection on the ground adiabatic state. (c) Probability of transmission on the excited adiabatic states. Blue circles are the SHEEP results, FSSH is given by red squares, and MF is given by black triangles.

For the current model problem, the lower excited state is not energetically accessible in the asymptotic region until $k > 13.4$ a.u. (the point at which the SHEEP and FSSH probabilities become non-zero, as seen in Fig. 5.3c). The MF method, however, gives

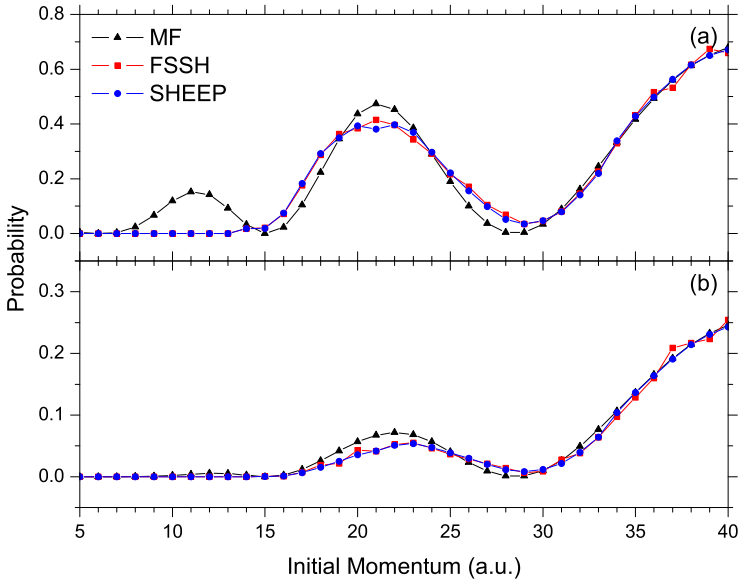

Figure 5.4: Three states with multiple avoided crossings model. (a) Probability of transmission on the first excited adiabatic state. (b) Probability of transmission on the second excited adiabatic state.

significant population in the excited states below this barrier, which stems from the wave function being restricted to a single Hartree product. [33] The other advantage is the previously mentioned ability to describe divergent reaction pathways. FSSH and SHEEP show both reflection and transmission at initial energies below the barrier to the excited states, while MF can only describe one result or the other at a time.

The second model problem we studied consists of a light particle coupled by a spring to a heavy particle sitting in a harmonic potential. This particular problem has been shown to be troublesome for surface hopping approaches while well suited for MF dynamics because there is constant coupling between states for all times. [52] Explicit details of the problem can be found in ref. [52] Figure 5.5 shows the potential energy curves for the model. The heavy particle has a mass of 10 a.u., and the light

particle has a mass of unity. The potential energy curves are given by

$$V_n(R) = \frac{1}{2}K_{sc}R^2 + (n + \frac{1}{2})\sqrt{k_{sc}/m}, \tag{5.8}$$

where K_{sc} is the spring constant for the external potential felt by the heavy particle ($K_{sc} = 15$ a.u.), n is the state index starting at zero, k_{sc} is the spring constant for the coupling between the light and heavy particles ($k_{sc} = 5$ a.u.), and m is the mass of the light particle. All trajectories were started on the ground state at $R = -0.75$ a.u. with zero initial momentum (the position of the circle in Fig. 5.5). This gives the particle a maximum kinetic energy of $\frac{1}{2}15(-0.75)^2 = 4.21875$ a.u., while the spacing between states is $\sqrt{5} \approx 2.23607$ a.u., slightly more than half the maximum kinetic energy. Again, 2000 trajectories were averaged together for the surface hopping based approaches, and 10 adiabatic states were included in the calculation.

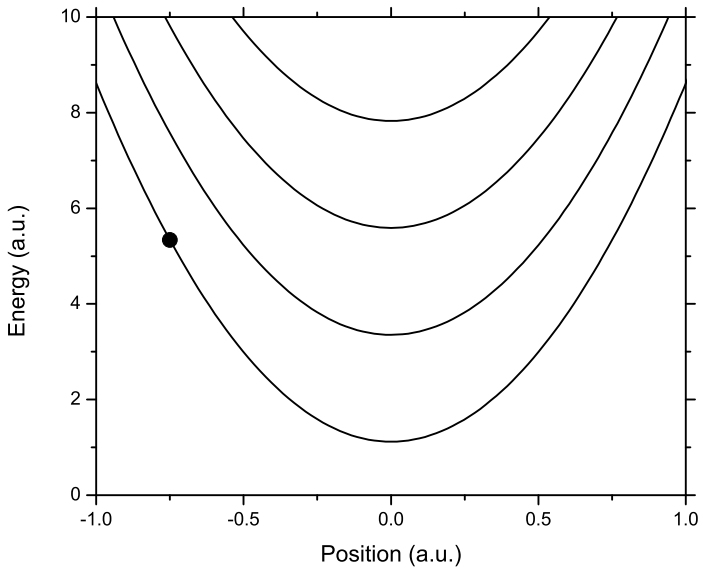

Figure 5.5: Harmonic oscillator with equally spaced excited states model. Adiabatic potential energy curves as a function of the nuclear coordinate. The circle shows the initial position for the trajectories.

Time evolution of the ground state population is displayed in Fig. 5.6. In general SHEEP is in good agreement with FSSH; however, SHEEP does show an increased dampening of the oscillations in the population. Even with the dampening, the SHEEP population oscillations remain mostly in phase with the FSSH oscillations. The dampening of the population oscillation for the surface hopping methods as compared to the MF dynamics is due to a loss of coherence between the members of the ensemble that constitute the surface hopping results. [52] The loss of coherence occurs more quickly with SHEEP in this case due to the dependence of the mean-field excited state PES on the history of the trajectory. Therefore, in addition to each trajectory having a different history of random hops, each trajectory also experience a slightly different PES for the excited state.

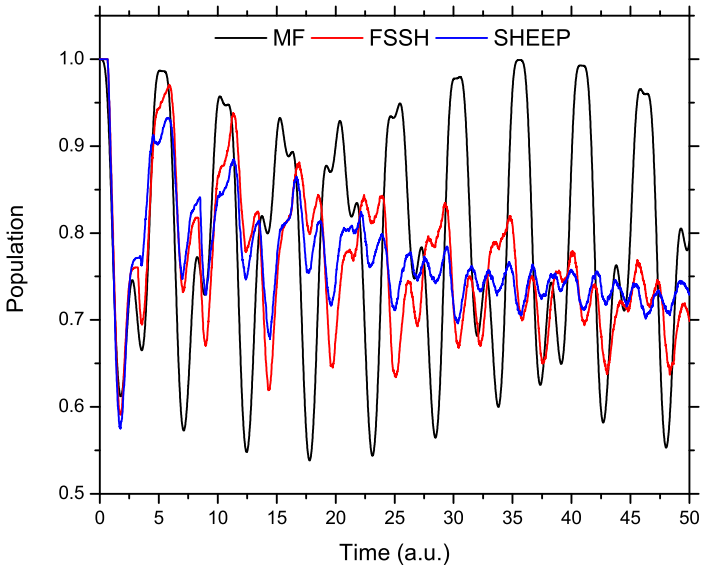

Figure 5.6: Harmonic oscillator with equally spaced excited states model. Time evolution of the ground state population. Loss of coherence between members of the ensembles causes the dampening of the oscillations for the surface hopping results.

The loss of coherence can also be seen in Fig. 5.7 where we have plotted the

average position and momentum of the heavy particle as functions of time. Through approximately the first half oscillation, all three methods agree. After that the surface hopping methods begin to become out of phase with the MF results, in addition to decreasing the amplitude of the oscillation. The average position and momentum from the surface hopping methods are approaching zero as the independent trajectories of the ensembles spread in phase space. SHEEP approaches zero more quickly because of the addition of the variances in the excited PES for each trajectory.

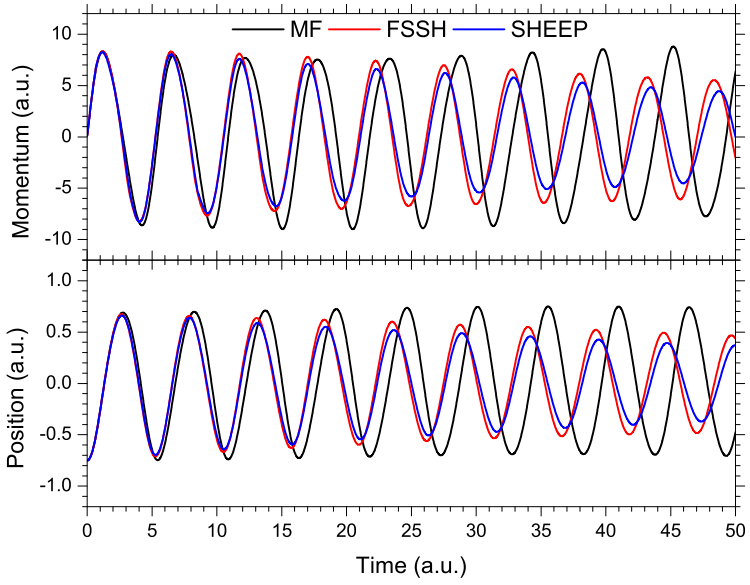

Figure 5.7: Harmonic oscillator with equally spaced excited states model. Time evolution of the average momentum (top panel) and position (bottom panel) of the heavy particle. Spreading of the trajectories in phase space causes the approach of the averages towards zero for SHEEP and FSSH.

Overall, the performance of SHEEP for this problem is rather encouraging. It has already been established that surface hopping methods are not well suited for a problem with non-vanishing coupling between states. [52] This problem also provides no justification for the separation ansatz that SHEEP applies to the electronic wave

function when it comes to nuclear dynamics. While SHEEP cannot reproduce the FSSH result here, it provides a good approximation.

To illustrate that SHEEP performs even better as compared to FSSH when there is some physical motivation for the separation ansatz, we modified the previous model to cluster the excited states closer together. A chemical analog of such system is a harmonic vibration with electronic excited states broadened by solvents. Specially we have decreased the excited state separation to one tenth of the separation between the ground state and first excited state as shown in Fig. 5.8. The remaining details of the problem were left unchanged (i.e. same non-adiabatic couplings, masses, initial conditions, and number of trajectories); although, we did include 15 states in these calculations to be sure we obtained a converged result with respect to the number of states.

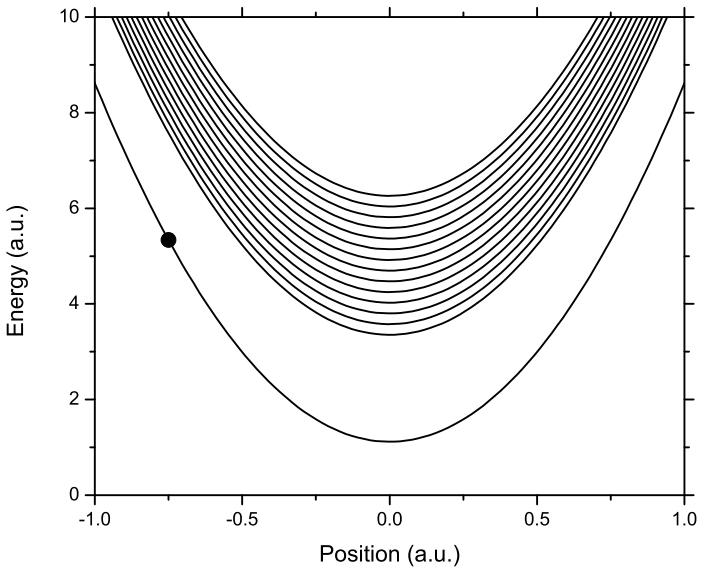

Figure 5.8: Harmonic oscillator with a dense manifold of excited states model. Adiabatic potential energy curves as a function of the nuclear coordinate. The circle shows the initial position for the trajectories.

Ground state population evolutions are shown in Fig. 5.9. Grouping the excited states together has led to the FSSH and SHEEP results agreeing with each other to a higher degree. There still exists the damped oscillation relative to the MF dynamics due to the loss of coherence, but now SHEEP and FSSH show similar dampening and fluctuations. The loss of coherence is again illustrated by the average position and momentum approaching zero as seen in Fig. 5.10. Modifying the excited state spacing has resulted in the SHEEP and FSSH phase space dynamics becoming more similar. The ensembles lose coherence at approximately the same rate now. While neither surface hopping based method does a particularly good job describing the dynamics of this model, the important item to note for us is that SHEEP performs no worse than FSSH here.

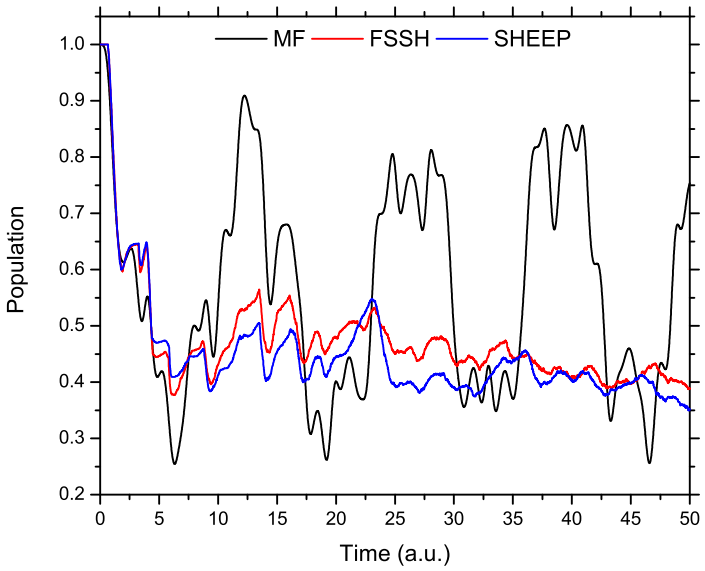

Figure 5.9: Harmonic oscillator with a dense manifold of excited states model. Time evolution of the ground state population. Bringing the excited states closer together brings the SHEEP and FSSH results closer together.

The final model problem we have examined was created with atom/surface inter-

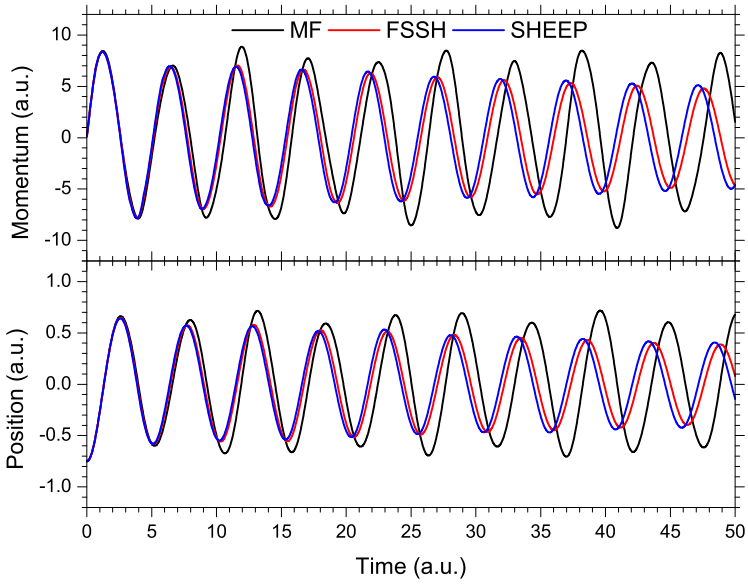

Figure 5.10: Harmonic oscillator with a dense manifold of excited states model. Time evolution of the average momentum (top panel) and position (bottom panel) of the heavy particle.

actions in mind. It consists of a ground state separated from 29 closely spaced and nearly parallel excited states. Figure 5.11 displays the diabatic and adiabatic potential energy curves for this problem. The matrix elements of the electronic Hamiltonian in the diabatic representation are

$$H_{11}(R) = 0.38(1 - \exp(-(1 - R)))^2 \tag{5.9a}$$

$$H_{nn}(R) = \exp(-2R) + \frac{n-2}{100} \tag{5.9b}$$

$$H_{1n}(R) = H_{n1}(R) = 0.05\exp(-(R - x_n)^2) \tag{5.9c}$$

$$H_{nm}(R) = H_{mn}(R) = 0.0 \tag{5.9d}$$

where x_n is the crossing point of H_{11} and H_{nn}. For this problem the classical particle had a mass of 2000 a.u. and started at $R = 1$ a.u. on the ground state. The initial momentum of the particle ranged from 20 to 50 a.u., and 1000 trajectories were

sampled for the FSSH and SHEEP results.

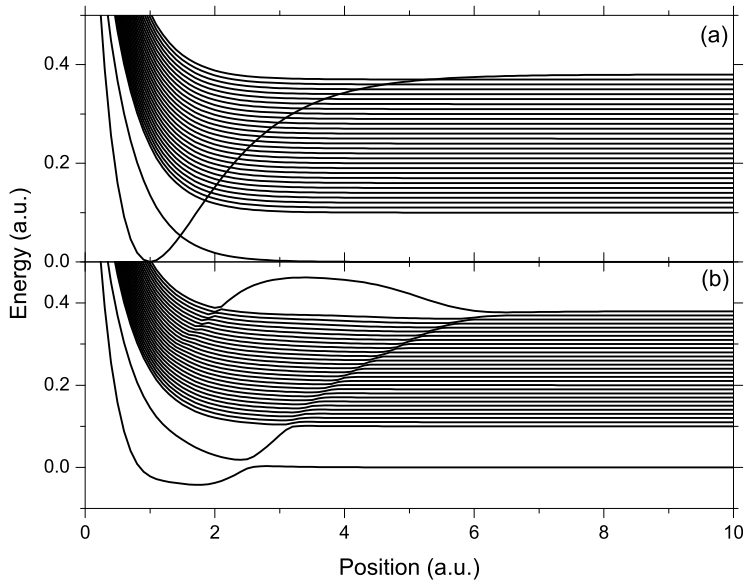

Figure 5.11: Thirty states with avoided crossings model. (a) Diabatic potential energy curves as a function of nuclear coordinate. (b) Adiabatic potential energy curves as a function of the nuclear coordinate.

In Fig. 5.12 are the probabilities for ending up on the ground adiabatic state in the asymptotic positive R region as a function of the initial momentum. Similar to the first model problem, the three methods generally agree at higher energies. At lower energies there are substantial differences between MF and SHEEP/FSSH, while the two surface hopping approaches are in qualitative agreement across the energy range. SHEEP appears to favor the ground state at lower energies. This most likely is due to the mean-field excited state energy being raised by contributions from higher-lying adiabatic states. This could result in hops being rejected due to a lack of kinetic energy, while FSSH predicts hops to low-lying excited states that are energetically allowed.

Testing SHEEP on a series of model problems has shown that the method can

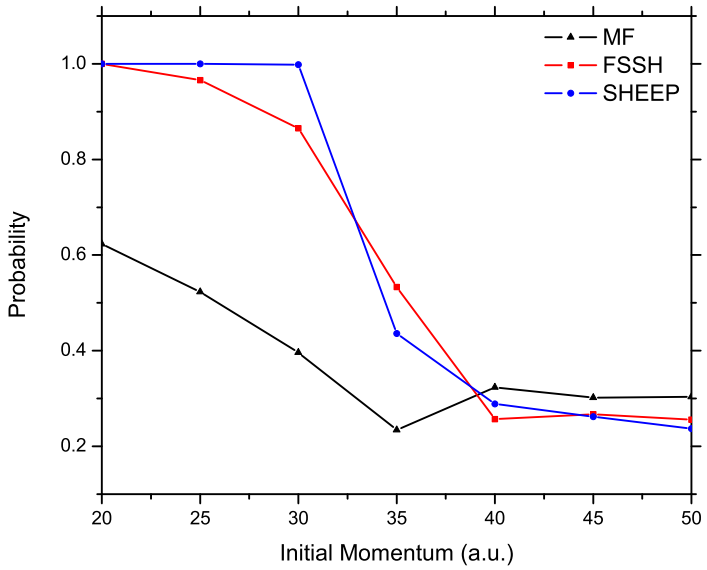

Figure 5.12: Thirty states with avoided crossings model. Probability of transmission on the ground adiabatic state as a function of initial momentum.

accurately reproduce the FSSH result without having to explicitly consider each excited state, particularly when there is some physical motivation for the separation ansatz. As seen with the last model problem, there will be situations where SHEEP will artificially favor the ground state. This short coming of SHEEP will be explored more in the next section.

5.3 Boltzmann equilibrium populations

With the previous model problems we analyzed the ability of SHEEP to reproduce the short time and scattering results of FSSH. Another area where FSSH has been shown to perform well is in obtaining nearly Boltzmann equilibrium populations of the electronic states. [70, 78] Specifically, it was found that FSSH exactly reproduces the Boltzmann populations in the limit of small adiabatic state splitting and in the

limit of large non-adiabatic coupling. In contrast, Ehrenfest dynamics only achieves Boltzmann populations in the high temperature limit and does very poor at lower temperatures. [70] Given that SHEEP is a combination of these two methods, it is important to determine where the performance of SHEEP lies.

To address this, we have devised our own version of the model problem used to test FSSH and Ehrenfest. This model consists of a linear chain of classical particles connected by anharmonic springs to each other. These particles act as a heat bath for the end particle, which is coupled to our multilevel quantum system. We designed our quantum energy levels to resemble what one might find in a semiconductor: relatively large energy gap between ground and excited states with significantly smaller energy gaps between excited states.

We followed the work of Tully and co-workers [70] and used a linear chain of 20 classical particles interacting via a nearest-neighbor potential energy function,

$$V(R) = \sum_{k=1}^{20} V_M(R_k - R_{k+1}), \tag{5.10}$$

where

$$V_M(R) = V_0 \left(a^2 R^2 - a^3 R^3 + 0.58 a^2 R^4\right) \tag{5.11}$$

with R_{21} being a fixed position and R_1 being the coordinate corresponding to the classical particle coupled to the quantum system. In addition to the purely classical particles as a heat bath, we applied a Langevin friction and random force to the 20th particle in the chain. The random force term is a Gaussian random variable with zero mean and a width given by

$$\sigma = \sqrt{2 k_b T \gamma M}, \tag{5.12}$$

where γ is the friction coefficient and M is the mass of the classical particle. We used the same parameters for the classical subsystem as Tully, [70] which are listed in Table 5.3 along with the parameters for our quantum subsystem. The classical equations of motion were integrated using the second-order method of Vanden-Eijnden

and Ciccotti [87], which reduces to the velocity Verlet algorithm if there is no friction or random force.

The quantum system consisted of 10 adiabatic states whose energies are given by

$$H_{nn} = \left(n + \frac{1}{2}\right)\hbar\sqrt{\frac{k_n}{m_e}} + E_{off}u(n-2) \tag{5.13}$$

where n runs from 0 to 9, k_n is a state-dependent force constant, E_{off} is an energy offset, and $u(n-2)$ is the Heaviside function. The quantum system was inspired by the electronic structure of a semiconductor where there is a substantial energy gap between ground and excited states ($\sim$ 1 eV) with significantly smaller energy gaps between excited states ($\sim$ 25 meV). The quantum potentials are independent of the classical coordinate, and all excited states are equally spaced. The non-adiabatic couplings for this harmonic system are given by

$$d_{nm} = \frac{2^{m+1}(m+1)!\delta_{nm+1}}{2\sqrt{2^{n+m}n!m!\alpha_{max(n,m)}}} - \frac{m2^{m-1}(m-1)!\delta_{nm-1}}{\sqrt{2^{n+m}n!m!\alpha_{max(n,m)}}}, \tag{5.14}$$

where $\alpha_{max(n,m)} = \sqrt[4]{\frac{m_e k_{max(n,m)}}{\hbar^2}}$. The density matrix equation of motion was integrated using a fourth-order Runge-Kutta method. Because Runge-Kutta methods are non-symplectic integrators, they don't maintain the idempotency of the density matrix without a very small time step. To circumvent this, we applied a McWeeny purification scheme [61] to maintain the idempotency of the density matrix. Both the classical and quantum propagations utilized a 10^{-2} fs time step. For this problem 200 trajectories were computed, each 800 ps in length with the first 500 ps discarded for equilibration.

Shown in Fig. 5.13 are the ground state populations as a function of system temperature. SHEEP shows reasonable agreement with the Boltzmann populations across the whole temperature range. We should note that SHEEP will not continue to show such good agreement as more excited states are added to the problem. This is a different manifestation of the problem that plauges the Ehrenfest method when looking at equilibrium populations.

Parameter	Value
V_0	175 kJ/mol
a	4 $Å^{-1}$
M	12 amu
γ	10^{14} s^{-1}
E_{off}	$1.5\hbar\left(\sqrt{\frac{k_1}{m_e}}-\sqrt{\frac{k_2}{m_e}}\right)$
k_n	$\begin{cases} 1.35\text{x}10^{-3}\frac{E_h}{a_0^2} & \text{if } n<2 \\ 8.44\text{x}10^{-7}\frac{E_h}{a_0^2} & \text{if } n\geq 2, \end{cases}$

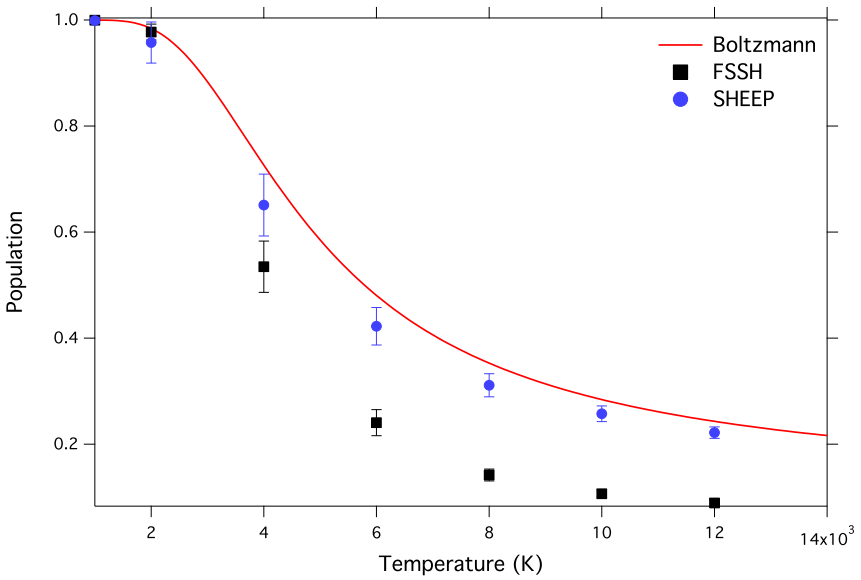

Figure 5.13: Ground state population as a function of temperature. The red line is the Boltzmann result, the black squares are the FSSH results, and the blue circles are the SHEEP results. The error bars represent the standard deviations of the population averages.

For Ehrenfest dynamics, all states have nearly equal population at all temperatures. As a consequence of this population behavior, the mean quantum energy in Ehrenfest dynamics scales linearly with the number of states. [71] In regards to

SHEEP this means that as more states are added, our mean-field excited state will increase in energy and trap our population in the ground state as the difference in potential energy between the ground state and mean-field excited state exceeds the kinetic energy of the classical particles. If we are only interested in the relaxation to the ground state at low temperatures (i.e. room temperature), then this drawback should only be a minor concern. In this type of calculation, the excited state is typically the starting point, and at these temperatures the system would lack the kinetic energy to overcome the fundamental band gap to repopulate the excited state after relaxation to the ground state.

One surprising result of the calculation is the poor performance of FSSH. It has been demonstrated previously, through both simulation and analytical expressions, that FSSH should at least be capable of a good approximation to the Boltzmann populations. [70, 78, 85] Upon further examination, we determined that the failing of FSSH in this problem relates to the structure of the energy levels for this particular problem and one aspect of the hopping algorithm. In the previous tests of FSSH with respect to Boltzmann populations, the model problems were either two level systems or multilevel systems where there was equal spacing of all the quantum states. The excited states in our problem are two orders of magnitude closer to each other than they are to the ground state. This causes problems for FSSH because the hopping algorithm that adds hopping probabilities together and tests for hops in an ascending manner.

For example if we are in the first excited state, we hop to the ground state if the hopping probability for a transition from the first excited state to the ground state is larger than the random number. If the random number is larger, we then look to hop to the second excited state. We will hop to the second excited state if the hopping probability for a transition from the first excited state to the second excited state plus the hopping probability for a transition from the first excited state to the ground state is greater than the random number, and so on. For the previous model

problems this posed no problem since hopping probabilities are typically very small, and thus you would need to add several together before the total hopping probability would be greater than the random number. By the time several were added together, you would be looking at hopping to a state several above the one currently occupied, which if the energy levels are equally space, meant that the potential energy change would be much larger than the kinetic energy.

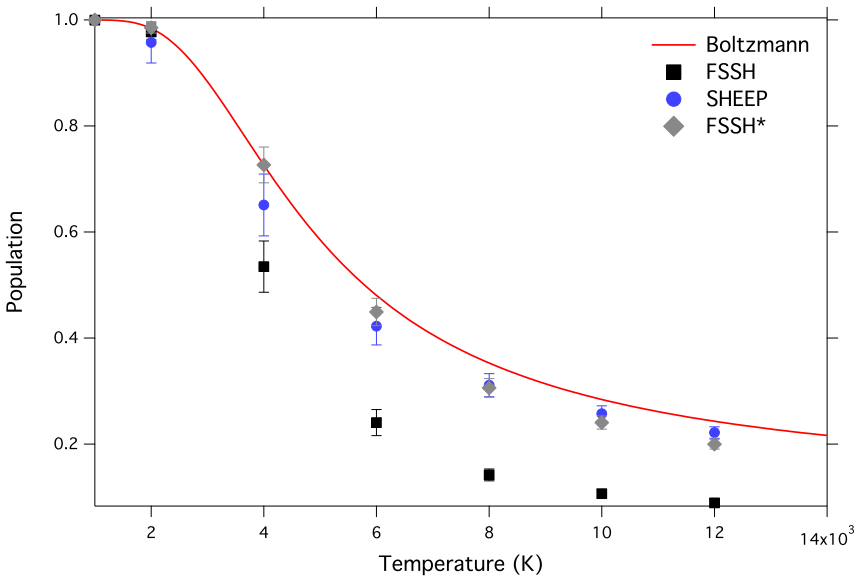

Figure 5.14: Ground state population as a function of temperature. The red line is the Boltzmann result, the black squares are the FSSH results, the blue circles are the SHEEP results, and the gray diamonds are the modified FSSH results. The error bars represent the standard deviations of the population averages.

In our model problem, however, the temperatures required to see significant equilibrium population in states other than the ground state are extremely high temperatures for the excited state energy spacing. Therefore, these hops that would have been rejected based on energy conservation in the previous model problems are accept in our model problem. In essence the hopping algorithm is trapping the population in the excited state, and we see lower than expected population in the ground state, especially as the temperature increases.

To verify this line of reasoning, we performed another set of FSSH calculations where we randomly decided at every time step the first state to which we would attempt to hop. We then cycled up from that state until all states were tested, or a hop was called predicted. As an example, if our randomly chosen first state to test was the fourth state out of five, we would test in the order 4, 5, 1, 2, 3. These results are shown in Fig. 5.14, labeled as FSSH*. This modification immediately improves the results, and they are now essentially the same as the results of SHEEP, if not slightly better. This shortcoming of FSSH was not anticipated and warrants further investigation as to the extent of the problem on the accuracy of results for other problems and the best remedy for the problem.

5.4 Approximations for SHEEP

SHEEP was developed in an attempt to lower the cost of surface hopping calculations, with application to a specific class of systems in mind. In developing and testing SHEEP, we have discovered that the structure of SHEEP lends itself to a few additional approximations that could potentially save a significant amount of computational time while at the same time having minimal impact on the accuracy. The first of these is similar in spirit to the classical path approximation that we made in implementing FSSH with electronic structure calculations.

For most applications of SHEEP, we would be concerned with simulating the relaxation of an excited electron back to the ground state. In most of these simulations, the initial excitation is not simulated; the system is simply started in the excited state of interest. Additionally, most of these simulations are performed around room temperature. For a semiconductor with a band gap of 1 eV, the Boltzmann factor at room temperature for population of the excited state is on the order of 10^{-17}. This means that once the system relaxes to the ground state, it will essentially never repopulate the excited state based solely on thermal energy.

SHEEP can take full advantage of this situation. Instead of needing to com-

pute hundreds of trajectories to simulate the relaxation dynamics in a system with a substantial band gap (i.e. the systems for which SHEEP was designed), we can pre-compute a single trajectory on which we can then sample the hopping dynamics and obtain the relaxation rate. While this would still not be on the same level of computational savings as the classical path approximation used earlier, we would still obtain significant savings over the standard surface hopping procedure. Note, this would not be possible with FSSH. Excited state energy spacings are typically the same order of magnitude as thermal energy fluctuations at room temperature in semiconductors; therefore, we would still need to compute individual trajectories in order to keep track of the excited state dynamics in FSSH.

Additionally, this would be a very well controlled approximation in SHEEP. By neglecting any transitions out of the ground state, we know *a priori* that our calculated relaxation rate will be an upper limit on the rate that would be computed with the full SHEEP procedure. The Boltzmann factor also provides a convenient measure of how well we can expect the approximation to perform as we either decrease the band gap or increase the system temperature.

A second tactic that could make for easier implementation and save some computational time is to approximate the excited mean-field state by the full mean-field state. The direct expression for the excited mean-field state force (Eq. 5.3) would involve excited state properties, the calculation of which we would like to avoid. The alternative offered above was a finite difference approach. While this avoids the excited state properties, it would still significantly increase computational costs.

By making use of the full mean-field state (for which we already have an analytical expression of the force in terms of a superposition state [55]) instead of the excited mean-field state, we would simplify the calculation of the force without significantly changing the dynamics provided that there are a large number of states. The ground state contribution to the full mean-field state will be inversely proportional to the number of states, on average. Assuming we do not start in a state that is strongly

coupled to the ground state, the dynamics of the full mean-field state and the excited mean-field state will be approximately the same when the number of states is large.

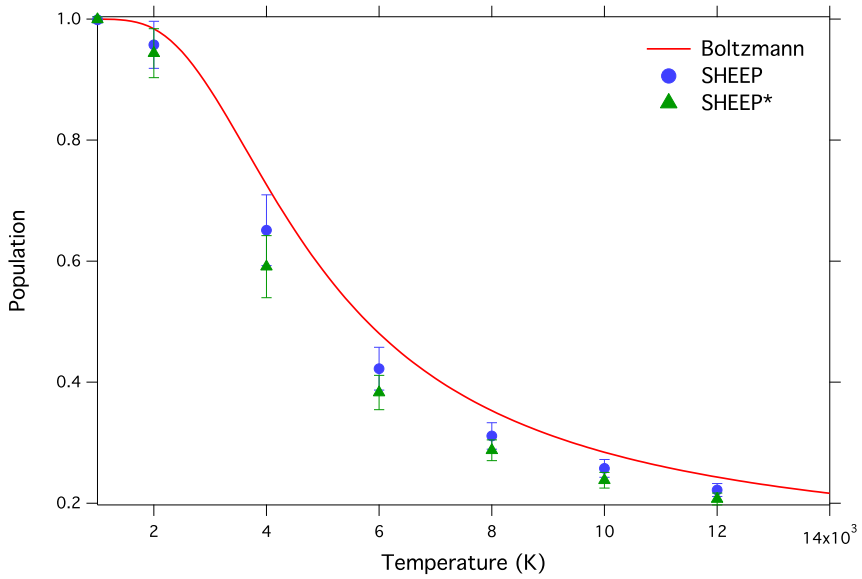

Figure 5.15: Ground state population as a function of temperature. The red line is the Boltzmann result, the blue circles are the SHEEP results, and the green triangles are the modified SHEEP results. The error bars represent the standard deviations of the population averages.

As a demonstration of the accuracy of this approximation, we have repeated the calculation of the previous section. Given in Fig. 5.15 are the ground state populations as a function of temperature for the original version of SHEEP and using the full mean-field state instead of the excited mean-field state (labeled SHEEP*). The results are in very good agreement for every temperature even for this model where there are only 10 states.

SHEEP is a very promising method for the simulation of the non-adiabatic dynamics of large systems. Making use of the approximation discussed here would reduce the computational burden of non-adiabatic dynamics even further. Whereas before we were forced to utilize a single determinant framework along with the classical path approximation in order to carry out surface hopping simulations, we now have the

potential to do essentially the same calculation on the excited state PES with a more complete description of the electronic structure.

BIBLIOGRAPHY

[1] A. P. Alivisatos. Semiconductor clusters, nanocrystals, and quantum dots. *Science*, 271:933–937, 1996.

[2] V. I. Arkhipov and H. Bassler. Exciton dissociation and charge photogeneration in pristine and doped conjugated polymers. *Phys. Status Solidi A*, 201:1152–1187, 2004.

[3] E Badaeva, J.W. May, J. Ma, D R Gamelin, and X Li. Characterization of Excited-State Magnetic Exchange in Mn^{2+}–Doped ZnO Quantum Dots Using Time-Dependent Density Functional Theory. *The Journal of Physical Chemistry C*, 2011.

[4] Ekateriana Badaeva, Yong Feng, Daniel R. Gamelin, and Xiaosong Li. Investigation of pure and co^{2+}-doped zno quantum dot electronic structures using the density functional theory: choosing the right functional. *New J. Phys.*, 10:055013, 2008.

[5] Ekateriana Badaeva, Christine M. Isborn, Yong Feng, Stefan T. Ochsenbein, Daniel R. Gamelin, and Xiaosog Li. Theoretical characterization of electronic transitions in co^{2+}- and mn^{2+}-doped zno nanocrystals. *J. Phys. Chem. C*, 113(20):8710–8717, 2009.

[6] Ekaterina Badaeva, Joseph W. May, Jiao Ma, Daniel R. Gamelin, and Xiaosong Li. Characterization of excited-state magnetic exchange in mn^{2+}-doped zno quantum dots using time-dependent density functional theory. *J. Phys. Chem. C*, 115(43):20986–20991, 2011.

[7] R Beaulac, PI Archer, and DR Gamelin. Luminescence in colloidal Mn^{2+}-doped semiconductor nanocrystals. *J. Solid State Chem.*, 181(7):1582–1589, 2008.

[8] M. J. Bedard-Hearn, R. E. Larsen, and B. J. Schwartz. Mean-field dynamics with stochastic decoherence (mf-sd): A new algorithm for nonadiabatic mixed quantum/classical molecular-dynamics simulations with nuclear-induced decoherence. *J. Chem. Phys.*, 123:234106, 2005.

[9] M. Ben-Nun, J. Quenneville, and T. J. Martinez. Ab initio multiple spawning: Photochemistry from first principles quantum molecular dynamics. *J. Phys. Chem. A*, 104(22):5161–5175, 2000.

[10] E. R. Bittner and P. J. Rossky. Quantum decoherence in mixed quantum-classical systems - nonadiabatic processes. *J. Chem. Phys.*, 103:8130–8143, 1995.

[11] M. Born and R. Oppenheimer. Zur quantentheorie der molekeln. *Ann. Phys.*, 84:457, 1927.

[12] C. J. Brabec, C. Winder, N. S. Sariciftci, J. C. Hummelen, A. Dhanabalan, P. A. van Hal, and R. A. Janssen. A low-bandgap semiconducting polymer for photovoltaic devices and infrared emitting diodes. *Adv. Funct. Mater.*, 12:709–712, 2002.

[13] M Bruchez, M Moronne, P Gin, S Weiss, and AP Alivisatos. Semiconductor nanocrystals as fluorescent biological labels. *Science*, 281(5385):2013–2016, 1998.

[14] SA Carter, JC Scott, and PJ Brock. Enhanced luminance in polymer composite light emitting devices. *Appl. Phys. Lett.*, 71(9):1145–1147, 1997.

[15] Joseph J Cavaleri, David E Skinner, D Philip Colombo, and Robert M Bowman. Femtosecond study of the size-dependent charge carrier dynamics in ZnO nanocluster solutions. *The Journal of Chemical Physics*, 103(13):5378, 1995.

[16] WCW Chan and SM Nie. Quantum dot bioconjugates for ultrasensitive nonisotopic detection. *Science*, 281(5385):2016–2018, 1998.

[17] WY Choi, A Termin, and MR Hoffmann. Effects of Metal-Ion Dopants on the Photocatalytic Reactivity of Quantum-Sized Tio2 Particles. *Angew Chem. Int. Edit.*, 33(10):1091–1092, 1994.

[18] WY Choi, A Termin, and MR Hoffmann. The Role of Metal-Ion Dopants in Quantum-Sized Tio2 - Correlation Between Photoreactivity and Charge-Carrier Recombination Dynamics. *J. Phys. Chem.*, 98(51):13669–13679, 1994.

[19] D. F. Coker and L. Xiao. Methods for molecular-dynamics with nonadiabatic transitions. *J. Chem. Phys.*, 102:496–510, 1995.

[20] V. L. Colvin, MC Schlamp, and AP Alivisatos. Light-Emitting-Diodes Made From Cadmium Selenide Nanocrystals and a Semiconducting Polymer. *Nature*, 370(6488):354–357, 1994.

[21] C. F. Craig, W. R. Duncan, and O. V. Prezhdo. Trajectory surface hopping in the time-dependent kohn-sham approach for electron-nuclear dynamics. *Phys. Rev. Lett.*, 95:163001, 2005.

[22] AM Derfus, WCW Chan, and SN Bhatia. Intracellular delivery of quantum dots for live cell labeling and organelle tracking. *Adv. Mater.*, 16(12):961–966, 2004.

[23] T. Dietl, P. Peyla, W. Grieshaber, and Y. Merle d'Aubigné. Dynamics of spin organization in diluted magnetic semiconductors. *Phys. Rev. Lett.*, 74:474–477, 1995.

[24] A. Dreuw and M. Head-Gordon. Single-reference ab initio methods for the calculation of excited states of large molecules. *Chem. Rev.*, 105:4009–4037, 2005.

[25] W. R. Duncan, C. F. Craig, and O. V. Prezhdo. Time-domain ab initio study of charge relaxation and recombination in dye-sensitized tio2. *J. Am. Chem. Soc.*, 129:8528–8543, 2007.

[26] Yong Feng, Ekaterina Badaeva, Daniel R. Gamelin, and Xiaosong Li. Excited-state double exchange in manganese-doped zno quantum dots: A time-dependent density-functional study. *J. Phys. Chem. Lett.*, 1(13):1927–1931, 2010.

[27] S. A. Fischer, W. R. Duncan, and O. V. Prezhdo. Ab initio nonadiabatic molecular dynamics of wet-electrons on the tio2 surface. *J. Am. Chem. Soc.*, 131:15483–15491, 2009.

[28] S. A. Fischer, B. F. Habenicht, A. B. Madrid, W. R. Duncan, and O. V. Prezhdo. Regarding the validity of the time-dependent kohn-sham approach for electron-nuclear dynamics via trajectory surface hopping. *J. Chem. Phys.*, 134:024102, 2011.

[29] Sean A. Fischer, Craig T. Chapman, and Xiaosong Li. Surface hopping with ehrenfest excited potential. *J. Chem. Phys.*, 135(14):144102, 2011.

[30] M. J. Frisch, G. W. Trucks, H. B. Schlegel, M. A. Robb G. E. Scuseria, J. R. Cheeseman, G. Scalmani, V. Barone, G. A. Petersson B. Mennucci, H. Nakatsuji, M. Caricato, X. Li, A. F. Izmaylov H. P. Hratchian, J. Bloino, G. Zheng, J. L. Sonnenberg, M. Ehara M. Hada, K. Toyota, R. Fukuda, J. Hasegawa, M. Ishida, Y. Honda T. Nakajima, O. Kitao, H. Nakai, T. Vreven, J. E. Peralta J. A. Montgomery Jr., F. Ogliaro, M. Bearpark, J. J. Heyd, K. N. Kudin E. Brothers, V. N. Staroverov, T. Keith, R. Kobayashi, K. Raghavachari J. Normand, A. Rendell, J. C. Burant, S. S. Iyengar, M. Cossi J. Tomasi, N. Rega, J. M.

Millam, M. Klene, J. E. Knox, V. Bakken J. B. Cross, C. Adamo, J. Jaramillo, R. Gomperts, O. Yazyev R. E. Stratmann, A. J. Austin, R. Cammi, C. Pomelli, R. L. Martin J. W. Ochterski, K. Morokuma, V. G. Zakrzewski, P. Salvador G. A. Voth, J. J. Dannenberg, S. Dapprich, N. J. Mayhall P. V. Parandekar, A. D. Daniels, Ö. Farkas, J. V. Ortiz J. B. Foresman, J. Cioslowski, and D. J. Fox. Gaussian Development Version Revision H.09+. Gaussian Inc., Wallingford CT 2011.

[31] M. J. Frisch, G. W. Trucks, H. B. Schlegel, M. A. Robb G. E. Scuseria, J. R. Cheeseman, G. Scalmani, V. Barone, G. A. Petersson B. Mennucci, H. Nakatsuji, M. Caricato, X. Li, A. F. Izmaylov H. P. Hratchian, J. Bloino, G. Zheng, J. L. Sonnenberg, M. Hada W. Liang, M. Ehara, K. Toyota, R. Fukuda, J. Hasegawa, T. Nakajima M. Ishida, Y. Honda, O. Kitao, H. Nakai, Jr. T. Vreven, J. A. Montgomery, J. E. Peralta, F. Ogliaro, J. J. Heyd M. Bearpark, E. Brothers, K. N. Kudin, V. N. Staroverov, R. Kobayashi T. Keith, J. Normand, K. Raghavachari, A. Rendell, S. S. Iyengar J. C. Burant, J. Tomasi, M. Cossi, N. Rega, J. M. Millam, J. E. Knox M. Klene, J. B. Cross, V. Bakken, C. Adamo, R. Gomperts J. Jaramillo, R. E. Stratmann, O. Yazyev, A. J. Austin, C. Pomelli R. Cammi, J. W. Ochterski, R. L. Martin, V. G. Zakrzewski K. Morokuma, G. A. Voth, P. Salvador, S. Dapprich J. J. Dannenberg, P. V. Parandekar, N. J. Mayhall, Ö. Farkas A. D. Daniels, J. B. Foresman, J. V. Ortiz, J. Cioslowski, and D. J. Fox. Gaussian Development Version Revision H.12+. Gaussian Inc., Wallingford CT 2011.

[32] M. J. Frisch, G. W. Trucks, H. B. Schlegel, G. E. Scuseria, M. A. Robb, J. R. Cheeseman, J. A. Montgomery, Jr., T. Vreven, K. N. Kudin, J. C. Burant, J. M. Millam, S. S. Iyengar, J. Tomasi, V. Barone, B. Mennucci, M. Cossi, G. Scalmani, N. Rega, G. A. Petersson, H. Nakatsuji, M. Hada, M. Ehara, K. Toyota, R. Fukuda, J. Hasegawa, M. Ishida, T. Nakajima, Y. Honda, O. Kitao, H. Nakai, M. Klene, X. Li, J. E. Knox, H. P. Hratchian, J. B. Cross, V. Bakken, C. Adamo, J. Jaramillo, R. Gomperts, R. E. Stratmann, O. Yazyev, A. J. Austin, R. Cammi, C. Pomelli, J. W. Ochterski, P. Y. Ayala, K. Morokuma, G. A. Voth, P. Salvador, J. J. Dannenberg, V. G. Zakrzewski, S. Dapprich, A. D. Daniels, M. C. Strain, O. Farkas, D. K. Malick, A. D. Rabuck, K. Raghavachari, J. B. Foresman, J. V. Ortiz, Q. Cui, A. G. Baboul, S. Clifford, J. Cioslowski, B. B. Stefanov, G. Liu, A. Liashenko, P. Piskorz, I. Komaromi, R. L. Martin, D. J. Fox, T. Keith, M. A. Al-Laham, C. Y. Peng, A. Nanayakkara, M. Challacombe, P. M. W. Gill, B. Johnson, W. Chen, M. W. Wong, C. Gonzalez, and J. A. Pople. Gaussian 03, Revision E.01. Gaussian, Inc., Wallingford, CT, 2004.

[33] R. B. Gerber, V. Buch, and M. A. Ratner. Time-dependent self-consistent field

approximation for intramolecular energy transfer. i. formulation and application to dissociation of van der waals molecules. *J. Chem. Phys.*, 77:3022–3030, 1982.

[34] G. Grancini, M. Maiuri, D. Fazzi, A. Petrozza, H.-J. Egelhaaf, D. Brida, G. Cerullo, and G. Lanzani. Hot exciton dissociation in polymer solar cells. *Nature Mater.*, 12:29–33, 2013.

[35] NC Greenham, XG Peng, and AP Alivisatos. Charge separation and transport in conjugated-polymer/semiconductor-nanocrystal composites studied by photoluminescence quenching and photoconductivity. *Phys. Rev. B*, 54(24):17628–17637, 1996.

[36] P. Guyot-Sionnest. Colloidal quantum dots. *C. R. Physique*, 9(8):777–787, 2008.

[37] B. F. Habenicht and O. V. Prezhdo. Time-domain ab initio study of nonradiative decay in a narrow graphene ribbon. *J. Phys. Chem. C*, 113:14067–14070, 2009.

[38] B. F. Habenicht and Prezhdo O. V. Nonradiative quenching of fluorescence in a semiconducting carbon nanotube: A time-domain ab initio study. *Phys. Rev. Lett.*, 100:197402, 2008.

[39] J. J. M. Halls, C. A. Walsh, N. C. Greenham, E. A. Marseglia, R. H. Friend, S. C. Moratti, and A. B. Holmes. Efficient photodiodes from interpenetrating polymer networks. *Nature*, 376:498–500, 1995.

[40] S. Hammes-Schiffer and J. C. Tully. Proton transfer in solution: Molecular dynamics with quantum transitions. *J. Chem. Phys.*, 101:4657–4667, 1994.

[41] E. J. Heller. Frozen gaussians: A very simple semi-classical approximation. *J. Chem. Phys.*, 75:2923–2931, 1981.

[42] C. Hu, O. Sugino, H. Hirai, and Y. Tateyama. Nonadiabatic couplings from the kohn-sham derivative matrix: formulation by time-dependent density-functional theory and evaluation in the pseudopotential framework. *Phys. Rev. A*, 82:062508, 2010.

[43] A. E. Jailaubekov, A. P. Willard, J. R. Tritch, W.-L. Chan, N. Sai, R. Gearba, L. G. Kaake, K. J. Williams, K. Leung, P. J. Rossky, and X.-Y. Zhu. Hot charge-transfer excitons set the time limit for charge separation at donor/acceptor interfaces in organic photovolatics. *Nature Mater.*, 12:66–73, 2013.

[44] JK Jaiswal, H Mattoussi, JM Mauro, and SM Simon. Long-term multiple color imaging of live cells using quantum dot bioconjugates. *Nat. Biotechnol.*, 21(1):47–51, 2003.

[45] Claire Johnson, Kevin Kittilstved, Tiffany Kaspar, Tim Droubay, Scott Chambers, G Salley, and Daniel Gamelin. Mid-gap electronic states in $Zn_{1x}Mn_xO$. *Phys. Rev. B*, 82(11), September 2010.

[46] Claire A Johnson, Tiffany C Kaspar, Scott A Chambers, G Mackay Salley, and Daniel R Gamelin. Sub-band-gap photoconductivity in Co^{2+}–doped ZnO. *Phys. Rev. B*, 81(12):125206, March 2010.

[47] Justin C Johnson, Kelly P Knutsen, Haoquan Yan, Matt Law, Yanfeng Zhang, Peidong Yang, and Richard J Saykally. Ultrafast Carrier Dynamics in Single ZnO Nanowire and Nanoribbon Lasers. *Nano. Lett.*, 4(2):197–204, February 2004.

[48] Prashant V Kamat. Quantum Dot Solar Cells. Semiconductor Nanocrystals as Light Harvesters. *J. Phys. Chem. C*, 112(48):18737–18753, 2008.

[49] S. V. Kilina, C. F. Craig, D. S. Kilin, and O. V. Prezhdo. Ab initio time-domain study of phonon-assisted relaxation of charge carriers in a pbse quantum dot. *J. Phys. Chem. C*, 111:4871–4878, 2007.

[50] S. V. Kilina, D. S. Kilin, and O. V. Prezhdo. Breaking the phonon bottleneck in pbse and cdse quantum dots: Time-domain density functional theory of charge carrier relaxation. *ACS Nano*, 3:93–99, 2009.

[51] Kevin R Kittilstved, William K Liu, and Daniel R Gamelin. Electronic structure origins of polarity-dependent high-TC ferromagnetism in oxide-diluted magnetic semiconductors. *Nat Mater*, 5(4):291–297, March 2006.

[52] D. Kohen, F. H. Stillinger, and J. C. Tully. Model studies of nonadiabatic dynamics. *J. Chem. Phys.*, 109:4713–4725, 1998.

[53] Anusorn Kongkanand, Kevin Tvrdy, Kensuke Takechi, Masaru Kuno, and Prashant V Kamat. Quantum dot solar cells. Tuning photoresponse through size and shape control of CdSe-TiO2 architecture. *J. Am. Chem. Soc.*, 130(12):4007–4015, 2008.

[54] DR Larson, WR Zipfel, RM Williams, SW Clark, MP Bruchez, FW Wise, and WW Webb. Water-soluble quantum dots for multiphoton fluorescence imaging in vivo. *Science*, 300(5624):1434–1436, 2003.

[55] Xiaosong Li, John C. Tully, H. Bernhard Schlegel, and Michael J. Frisch. Ab initio ehrenfest dynamics. *J. Chem. Phys.*, 123(8):084106, 2005.

[56] Tzarara Lopez-Luke, Abraham Wolcott, Li-ping Xu, Shaowei Chen, Zhenhai Wcn, Jinghong Li, Elder De La Rosa, and Jin Z. Zhang. Nitrogen-doped and CdSe quantum-dot-sensitized nanocrystalline TiO2 films for solar energy conversion applications. *J. Phys. Chem. C*, 112(4):1282–1292, 2008.

[57] P.-O. Löwdin. On the non-orthogonality problem connected with the use of atomic wave functions in the theory of molecules and crystals. *J. Chem. Phys.*, 18:365, 1950.

[58] N. T. Maitra. On correlated electron-nuclear dynamics using time-dependent density functional theory. *J. Chem. Phys.*, 125:014110, 2006.

[59] C. C. Martens and J. Y. Fang. Semiclassical-limit molecular dynamics on multiple electronic surfaces. *J. Chem. Phys.*, 106:4918–4930, 1997.

[60] A. D. McLachlan. Variational solution of time-dependent schrodinger equation. *Mol. Phys.*, 8:39–&, 1964.

[61] R. McWeeny. Some recent advances in density matrix theory. *Rev. Mod. Phys.*, 32:335–369, 1960.

[62] H. D. Meyer and W. H. Miller. Classical analog for electronic degrees of freedom in non-adiabatic collision processes. *J. Chem. Phys.*, 70:3214–3223, 1979.

[63] D. A. Micha. A self-consistent eikonal treatment of electronic-transitions in molecular collisions. *J. Chem. Phys.*, 78:7138–7145, 1983.

[64] D. A. Micha. Time-dependent many-electron treatment of electronic energy and charge transfer in atomic collisions. *J. Phys. Chem. A*, 103(38):7562, 1999.

[65] D. A. Micha and K. Runge. Time-dependent many-electron approach to slow ion-atom collisions - the coupling of electronic and nuclear motions. *Phys. Rev. A*, 50(1):322, 1994.

[66] W. H. Miller. Electronically nonadiabatic dynamics via semiclassical initial value methods. *J. Phys. Chem. A*, 113(8):1405, 2009.

[67] W. H. Miller and C. W. McCurdy. Classical trajectory model for electronically non-adiabatic collision phenomena - classical analog for electronic degrees of freedom. *J. Chem. Phys.*, 69:5163–5173, 1978.

[68] U. Müller and G. Stock. Surface-hopping modeling of photoinduced relaxation dynamics on coupled potential-energy surfaces. *J. Chem. Phys.*, 107:6230–6245, 1997.

[69] NS Norberg, KR Kittilstved, JE Amonette, RK Kukkadapu, DA Schwartz, and DR Gamelin. Synthesis of colloidal Mn^{2+}: ZnO quantum dots and high-T_C ferromagnetic nanocrystalline thin films. *Journal of the American Chemical Society*, 126(30):9387–9398, 2004.

[70] P. V. Parandekar and J. C. Tully. Mixed quantum-classical equilibrium. *J. Chem. Phys.*, 122:094102, 2005.

[71] P. V. Parandekar and J. C. Tully. Detailed balance in ehrenfest mixed quantum-classical dynamics. *J. Chem. Theor. Comput.*, 2:229–235, 2006.

[72] M. J. Paterson, P. A. Hunt, M. A. Robb, and O. Takahashi. Non-adiabatic direct dynamics study of chromium hexacarbonyl photodissociation. *J. Phys. Chem. A*, 106:10494–10504, 2002.

[73] P. Pechukas. Time-dependent semiclassical scattering theory. ii. atomic collisions. *Phys. Rev.*, 181:174–185, 1969.

[74] Rohit P. Prasankumar, Prashanth C. Upadhya, and Antoinette J. Taylor. Ultrafast carrier dynamics in semiconductor nanowires. *Phys Status Solidi B*, 246(9):1973–1995, 2009.

[75] O. V. Prezhdo. Mean field approximation for the stochastic schrodinger equation. *J. Chem. Phys.*, 111:8366–8377, 1999.

[76] A. Savin, C. J. Umrigar, and X. Gonze. Relationship of kohn-sham eigenvalues to excitation energies. *Chem. Phys. Lett.*, 288:391–395, 1998.

[77] MC Schlamp, XG Peng, and AP Alivisatos. Improved efficiencies in light emitting diodes made with CdSe(CdS) core/shell type nanocrystals and a semiconducting polymer. *J. Appl. Phys.*, 82(11):5837–5842, 1997.

[78] J. R. Schmidt, P. V. Parandekar, and J. C. Tully. Mixed quantum-classical equilibrium: surface hopping. *J. Chem. Phys.*, 129:044104, 2008.

[79] G. Stock and M. Thoss. Semiclassical description of nonadiabatic quantum dynamics. *Phys. Rev. Lett.*, 78:578–581, 1997.

[80] E. Tapavicza, I. Tavernelli, and U. Rothlisberger. Trajectory surface hopping within linear response time-dependent density-functional theory. *Phys. Rev. Lett.*, 98:023001, 2007.

[81] B. C. Thompson and M. J. Fréchet. Polymer-fullerene composite solar cells. *Angew. Chem., Int. Ed.*, 47:58–77, 2008.

[82] J. C. Tully. Molecular-dynamics with electronic-transitions. *J. Chem. Phys.*, 93:1061–1071, 1990.

[83] J. C. Tully. *Classical and Quantum Dynamics in Condensed Phase Simulations.* World Scientific, Singapore, 1998.

[84] J. C. Tully. Mixed quantum-classical dynamics. *Faraday Discuss.*, 110:407–419, 1998.

[85] J. C. Tully. Perspective: nonadiabatic dynamics theory. *J. Chem. Phys.*, 137:22A301, 2012.

[86] J. C. Tully and R. K. Preston. Trajectory surface hopping approach to nonadiabatic molecular collisions - reaction of h^+ with d_2. *J. Chem. Phys.*, 55:562–&, 1971.

[87] E. Vanden-Eijnden and G. Ciccotti. Second-order integrators for langevin equations with holonomic constraints. *Chem. Phys. Lett.*, 429:310–316, 2006.

[88] T. Vreven, F. Bernardi, M. Garavelli, M. Olivucci, M. A. Robb, and H. B. Schlegel. Ab initio photoisomerization dynamics of a simple retinal chromophore model. *J. Am. Chem. Soc.*, 119:12687–12688, 1997.

[89] SP Wang, N Mamedova, NA Kotov, W Chen, and J Studer. Antigen/antibody immunocomplex from CdTe nanoparticle bioconjugates. *Nano. Lett.*, 2(8):817–822, 2002.

[90] Y Wang and N Herron. Semiconductor nanocrystals in carrier-transporting polymers. Charge generation and charge transport. *J. Luminescence*, 70:48–59, 1996.

[91] F. Webster, P. J. Rossky, and R. A. Friesner. Nonadiabatic processes in condensed matter - semiclassical theory and implementation. *Comput. Phys. Commun.*, 63:494–522, 1991.

[92] C. Winder, G. Matt, J. C. Hummelen, R. A. Janssen, N. S. Sariciftci, and C. J. Brabec. Sensitization of low bandgap polymer bulk heterojunction solar cells. *Thin Solid Films*, 403:373–379, 2002.

[93] A. Wood, M. Giersig, M. Hilgendorff, A. Vilas-Campos, L. M. Liz-Marzán, and P. Mulvaney. Size effects in zno: the cluster to quantum dot transition. *Aust. J. Chem.*, 56:1051–1057, 2003.

[94] XY Wu, HJ Liu, JQ Liu, KN Haley, JA Treadway, JP Larson, NF Ge, F Peale, and MP Bruchez. Immunofluorescent labeling of cancer marker Her2 and other cellular targets with semiconductor quantum dots. *Nat. Biotechnol.*, 21(1):41–46, 2003.

[95] R. E. Wyatt and E. R. Bittner. Quantum wave packet dynamics with trajectories: Implementation with adaptive lagrangian grids. *J. Chem. Phys.*, 113:8898–8907, 2000.

[96] Harish Kumar Yadav, K Sreenivas, and Vinay Gupta. Study of metal/ZnO based thin film ultraviolet photodetectors: The effect of induced charges on the dynamics of photoconductivity relaxation. *J. Appl. Phys.*, 107(4):044507, 2010.

[97] G. Yu and A. J. Heeger. Charge separation and photovoltaic conversion in polymer composites with internal donor-acceptor heterojunctions. *J. Appl. Phys.*, 78:4510–4515, 1995.

[98] Y. Zhang, S.-C. Chien, K-S. Chen, H-L. Yip, Y. Sun, J. A. Davies, F.-C. Chen, and A. K.-Y. Jen. Increased open circuit voltage in fluorinated benzothiadiazole-based alternating conjugated polymers. *Chem. Commun.*, 47:11026–11028, 2011.

[99] Y. Zhang, J. Zou, H-L. Yip, K-S. Chen, D. F. Zeigler, Y. Sun, and A. K.-Y. Jen. Indacenodithiophene and quinoaxline-based conjugated polymers for highly efficient polymer solar cells. *Chem. Mater.*, 23:2289–2291, 2011.

Appendix A

DERIVATION OF EHRENFEST DYNAMICS

The following derivation follows that of Tully [83] Our starting point is the full time-dependent Schrödinger equation and a product ansatz for the total wave function:

$$i\hbar\frac{\partial}{\partial t}\Psi(\mathbf{r},\mathbf{R},t) = \hat{\mathcal{H}}(\mathbf{r},\mathbf{R})\Psi(\mathbf{r},\mathbf{R},t) \tag{A.1}$$

$$\Psi(\mathbf{r},\mathbf{R},t) = \Theta(\mathbf{r},t)\Omega(\mathbf{R},t)\exp\left[\frac{i}{\hbar}\int^{t} E_r(t')dt'\right] \tag{A.2}$$

where $E_r(t)$ is a phase factor inserted to simplify the final appearance of the equations and taken to be

$$E_r(t) = \left\langle \Theta(\mathbf{r},t)\Omega(\mathbf{R},t)\left|\hat{\mathcal{H}}_{el}(\mathbf{r},\mathbf{R})\right|\Theta(\mathbf{r},t)\Omega(\mathbf{R},t)\right\rangle_{r,R}. \tag{A.3}$$

The angle brackets refer to integration over the variable(s) given as a subscript. The Hamiltonian governing the system is given by

$$\hat{\mathcal{H}} = -\frac{\hbar^2}{2M}\nabla^2_{\mathbf{R}} - \frac{\hbar^2}{2m}\nabla^2_{\mathbf{r}} + V(\mathbf{r},\mathbf{R}) \tag{A.4a}$$

$$= -\frac{\hbar^2}{2M}\nabla^2_{\mathbf{R}} + \hat{\mathcal{H}}_{el}(\mathbf{r},\mathbf{R}) \tag{A.4b}$$

where M is the mass of the nucleus and m is the mass of the electron. An equation of motion for the electronic subsystem can be obtained by substituting Eq. A.2 into Eq. A.1, multiplying from the left by Ω^*, and integrating over $\mathbf{R}$:

$$i\hbar\frac{\partial}{\partial t}\Theta(\mathbf{r},t) = -\frac{\hbar^2}{2m}\nabla^2_{\mathbf{r}}\Theta(\mathbf{r},t) + \left\langle \Omega(\mathbf{R},t)\left|-\frac{\hbar^2}{2M}\nabla^2_{\mathbf{R}} + V(\mathbf{r},\mathbf{R})\right|\Omega(\mathbf{R},t)\right\rangle_{\mathbf{R}}\Theta(\mathbf{r},t)$$
$$+ E_r(t)\Theta(\mathbf{r},t) - i\hbar\left\langle \Omega(\mathbf{R},t)\left|\frac{\partial\Omega(\mathbf{R},t)}{\partial t}\right\rangle_{\mathbf{R}}\Theta(\mathbf{r},t). \right. \tag{A.5}$$

The process can be repeated analogously to obtain an effective equation for the nuclear subsystem:

$$i\hbar\frac{\partial}{\partial t}\Omega(\mathbf{R},t) = -\frac{\hbar^2}{2M}\nabla^2_{\mathbf{R}}\Omega(\mathbf{R},t) + \left\langle \Theta(\mathbf{r},t)\left|\hat{\mathcal{H}}_{el}(\mathbf{r},\mathbf{R})\right|\Theta(\mathbf{r},t)\right\rangle_{\mathbf{r}}\Omega(\mathbf{R},t) + E_r(t)\Omega(\mathbf{R},t) - i\hbar\left\langle \Theta(\mathbf{r},t)\left|\frac{\partial\Theta(\mathbf{r},t)}{\partial t}\right\rangle_{\mathbf{r}}\Omega(\mathbf{R},t). \quad \text{(A.6)}$$

The time derivative factors on the right hand side of Eqs. A.5 and A.6 can be chosen arbitrarily as long as they satisfy the equation for the total energy obtained via multiplying Eq. A.5 from the left by $\Theta^*(\mathbf{r},t)$ and integrating over $\mathbf{r}$ (or multiplying Eq. A.6 from the left by $\Omega^*(\mathbf{R},t)$ and integrating over $\mathbf{R}$),

$$i\hbar\left\langle \Theta(\mathbf{r},t)\left|\frac{\partial\Theta(\mathbf{r},t)}{\partial t}\right\rangle_{\mathbf{r}} + i\hbar\left\langle \Omega(\mathbf{R},t)\left|\frac{\partial\Omega(\mathbf{R},t)}{\partial t}\right\rangle_{\mathbf{R}} - E_r(t) = \left\langle \Theta(\mathbf{r},t)\Omega(\mathbf{R},t)\left|\hat{\mathcal{H}}(\mathbf{r},\mathbf{R})\right|\Theta(\mathbf{r},t)\Omega(\mathbf{R},t)\right\rangle_{\mathbf{r},\mathbf{R}} = E. \quad \text{(A.7)}$$

As we have not made a symmetric choice in separating variables, it will be advantageous to make an asymmetric choice in phase factors. We define them as follows:

$$i\hbar\left\langle \Omega(\mathbf{R},t)\left|\frac{\partial\Omega(\mathbf{R},t)}{\partial t}\right\rangle_{\mathbf{R}} = E, \quad \text{(A.8)}$$

$$i\hbar\left\langle \Theta(\mathbf{r},t)\left|\frac{\partial\Theta(\mathbf{r},t)}{\partial t}\right\rangle_{\mathbf{r}} = E_r(t). \quad \text{(A.9)}$$

By making use of Eqs. A.7, A.8, and A.9 in Eqs. A.5 and A.6, we arrive at the final equations that specify the TDSCF method:

$$i\hbar\frac{\partial}{\partial t}\Theta(\mathbf{r},t) = -\frac{\hbar^2}{2m}\nabla^2_{\mathbf{r}}\Theta(\mathbf{r},t) + \langle\Omega(\mathbf{R},t)\,|V(\mathbf{r},\mathbf{R})|\,\Omega(\mathbf{R},t)\rangle_{\mathbf{R}}\,\Theta(\mathbf{r},t), \quad \text{(A.10)}$$

$$i\hbar\frac{\partial}{\partial t}\Omega(\mathbf{R},t) = -\frac{\hbar^2}{2M}\nabla^2_{R}\Omega(\mathbf{R},t) + \left\langle \Theta(\mathbf{r},t)\left|\hat{\mathcal{H}}_{el}(\mathbf{r},\mathbf{R})\right|\Theta(\mathbf{r},t)\right\rangle_{r}\Omega(\mathbf{R},t). \quad \text{(A.11)}$$

The Ehrenfest method is obtained by taking the classical limit of Eq. A.11. This can be accomplished by writing the nuclear wave function in terms of an amplitude and a phase factor,

$$\Omega(\mathbf{R},t) = A(\mathbf{R},t)\exp\left[\frac{i}{\hbar}S(\mathbf{R},t)\right]. \quad \text{(A.12)}$$

In the above, $A(\mathbf{R},t)$ and $S(\mathbf{R},t)$ are both real-valued. Insertion of Eq. A.12 into Eq. A.11, followed by separating into real and imaginary parts, results in

$$\frac{\partial S(\mathbf{R},t)}{\partial t} + \frac{1}{2M}\left(\nabla_{\mathbf{R}} S(\mathbf{R},t)\right)^2 + \left\langle \Theta(\mathbf{r},t) \left| \hat{\mathcal{H}}_{el}(\mathbf{r},\mathbf{R}) \right| \Theta(\mathbf{r},t) \right\rangle_{\mathbf{r}} = \frac{\hbar^2}{2M} \frac{\nabla^2_{\mathbf{R}} A(\mathbf{R},t)}{A(\mathbf{R},t)} \quad \text{(A.13)}$$

$$\frac{\partial A(\mathbf{R},t)}{\partial t} + \frac{\nabla_{\mathbf{R}} A(\mathbf{R},t) \cdot \nabla_{\mathbf{R}} S(\mathbf{R},t)}{M} + \frac{A(\mathbf{R},t)}{2M} \nabla^2_{\mathbf{R}} S(\mathbf{R},t) = 0. \quad \text{(A.14)}$$

Taking the classical limit by setting $\hbar \to 0$, we obtain a Hamilton-Jacobi equation:

$$\frac{\partial S(\mathbf{R},t)}{\partial t} + \frac{1}{2M}\left(\nabla_{\mathbf{R}} S(\mathbf{R},t)\right)^2 + \left\langle \Theta(\mathbf{r},t) \left| \hat{\mathcal{H}}_{el}(\mathbf{r},\mathbf{R}) \right| \Theta(\mathbf{r},t) \right\rangle_{\mathbf{r}} = 0. \quad \text{(A.15)}$$

Equations A.14 and A.15 are now equivalent to Newton's equations of motion with a force derived from the expectation value of the electronic Hamiltonian,

$$M\ddot{\mathbf{R}} = -\nabla_{\mathbf{R}} \left\langle \Theta(\mathbf{r},t) \left| \hat{\mathcal{H}}_{el}(\mathbf{r},\mathbf{R}) \right| \Theta(\mathbf{r},t) \right\rangle_{\mathbf{r}} \quad \text{(A.16)}$$

The last step in obtaining the Ehrenfest method is to replace the nuclear wave function in Eq. A.10 with a delta function at the classical trajectory position:

$$i\hbar \frac{\partial}{\partial t} \Theta(\mathbf{r},t;\mathbf{R}) = \hat{\mathcal{H}}_{el}(\mathbf{r};\mathbf{R}) \Theta(\mathbf{r},t;\mathbf{R}) \quad \text{(A.17)}$$

where now the electronic wave function contains a parametric dependence on the nuclear coordinates. These last two equations define the Ehrenfest method.

Appendix B

DERIVATION OF FSSH

This derivation follows that of Tully [84] and parallels the Ehrenfest dynamics derivation. Instead of making use of a single product ansatz for the total wave function, as we did to derive Ehrenfest dynamics, we begin with a multi-configuration description:

$$\Psi(\mathbf{r},\mathbf{R},t) = \sum_i \Phi_i(\mathbf{r};\mathbf{R})\Omega_i(\mathbf{R},t). \tag{B.1}$$

Here Φ_i are orthonormal basis functions for the electrons, which can be adiabatic or diabatic. Insertion of Eq. B.1 into the time-dependent Schrödinger equation, followed by multiplication from the left by Φ_j^* and integration over $\mathbf{r}$ leads to a set of coupled equations for the nuclear wave functions,

$$\begin{aligned} i\hbar\frac{\partial}{\partial t}\Omega_j(\mathbf{R},t) = &-\frac{\hbar^2}{2M}\nabla_{\mathbf{R}}\Omega(\mathbf{R},t) + \sum_i H_{ji}(\mathbf{R})\Omega_i(\mathbf{R},t) \\ &+ \frac{\hbar^2}{2M}\sum_i \mathbf{D}_{ji}(\mathbf{R})\Omega_i(\mathbf{R},t) - \frac{\hbar^2}{M}\sum_{i\neq j}\mathbf{d}_{ji}(\mathbf{R})\cdot\nabla_{\mathbf{R}}\Omega_i(\mathbf{R},t). \end{aligned} \tag{B.2}$$

In the above, H_{ji} are matrix elements of the electronic Hamiltonian and $\mathbf{d}_{ji}$ and $\mathbf{D}_{ji}$ are the first and second derivative couplings, respectively:

$$H_{ji}(\mathbf{R}) = \left\langle \Phi_j(\mathbf{r};\mathbf{R}) \left| \hat{\mathcal{H}}_{el}(\mathbf{r};\mathbf{R}) \right| \Phi_i(\mathbf{r};\mathbf{R}) \right\rangle_{\mathbf{r}} \tag{B.3}$$

$$\mathbf{d}_{ji}(\mathbf{R}) = \left\langle \Phi_j(\mathbf{r};\mathbf{R}) \left| \nabla_{\mathbf{R}}\Phi_i(\mathbf{r};\mathbf{R}) \right\rangle_{\mathbf{r}} \right. \tag{B.4}$$

$$\mathbf{D}_{ji}(\mathbf{R}) = -\left\langle \Phi_j(\mathbf{r};\mathbf{R}) \left| \nabla^2_{\mathbf{R}}\Phi_i(\mathbf{r};\mathbf{R}) \right\rangle_{\mathbf{r}} \right. . \tag{B.5}$$

With a full expansion in Eq. B.1, Eq. B.2 is an exact solution to the time-dependent Schrödinger equation.

FSSH is a classical analogue of Eq. B.2 that seeks to capture the essential physics in a much more computationally friendly manner. This can be seen by treating Eq. B.2 similar to the way in which we treated the nuclear half of the time-dependent self-consistent field equations in the Ehrenfest derivation. First, we rewrite the the nuclear wave functions as

$$\Omega_j(\mathbf{R},t) = A_j(\mathbf{R},t)\exp\left[\frac{i}{\hbar}S_j(\mathbf{R},t)\right]. \tag{B.6}$$

Substituting this into Eq. B.2 will yield

$$\begin{aligned}\frac{\partial S_j(\mathbf{R},t)}{\partial t} &+ \frac{1}{2M}\left(\nabla_{\mathbf{R}}S_j(\mathbf{R},t)\right)^2 + H_{jj}(\mathbf{R}) \\ &= \frac{\hbar^2}{2M}\frac{\nabla^2_{\mathbf{R}}A_j(\mathbf{R},t)}{A_j(\mathbf{R},t)} - \sum_i \frac{\hbar^2}{2M}\frac{A_i(\mathbf{R},t)}{A_j(\mathbf{R},t)}\mathbf{D}_{ji}(\mathbf{R})\exp\left[\frac{i}{\hbar}(S_i(\mathbf{R},t)-S_j(\mathbf{R},t)\right] \\ &\quad + \frac{\hbar}{M}\sum_i \mathbf{d}_{ji}(\mathbf{R})\left(\frac{\nabla_{\mathbf{R}}A_i(\mathbf{R},t)}{A_j(\mathbf{R},t)}\right)\exp\left[\frac{i}{\hbar}(S_i(\mathbf{R},t)-S_j(\mathbf{R},t)\right]\end{aligned} \tag{B.7}$$

$$\begin{aligned}\frac{\partial A_j(\mathbf{R},t)}{\partial t} &+ \frac{1}{M}\nabla_{\mathbf{R}}A_j(\mathbf{R},t)\cdot\nabla_{\mathbf{R}}S_j(\mathbf{R},t) + \frac{1}{2M}A_j(\mathbf{R},t)\nabla^2_{\mathbf{R}}S_j(\mathbf{R},t) \\ &\quad + \sum_{i\neq j} A_i(\mathbf{R},t)\left\{\left[\frac{1}{M}\mathbf{d}_{ji}(\mathbf{R})\cdot\nabla_{\mathbf{R}}S_i(\mathbf{R},t)\right.\right. \\ &\quad \left.\left. + \frac{i}{\hbar}H_{ji}(\mathbf{R})\right]\exp\left[\frac{i}{\hbar}(S_i(\mathbf{R},t)-S_j(\mathbf{R},t)\right]\right\} = 0.\end{aligned} \tag{B.8}$$

We have purposely separated the diagonal term of the electronic Hamiltonian matrix from the off-diagonal terms. In doing so, we can take the classical limit of Eq. B.7 to obtain

$$\frac{\partial S_j(\mathbf{R},t)}{\partial t} + \frac{1}{2M}\left(\nabla_{\mathbf{R}}S_j(\mathbf{R},t)\right)^2 + H_{jj}(\mathbf{R}) = 0. \tag{B.9}$$

This equation is very reminiscent of the equation we obtained after taking the classical limit in the Ehrenfest derivation. The physics described by Eqs. B.9 and B.8 consists of motion on each PES with the amplitudes on each surface being modulated by the last term in Eq. B.8, which couples the surfaces together. This last term in Eq. B.8 closely resembles the equation of motion for the electronic wave function expansion

coefficients that we obtained in Chapter 1. FSSH then approximates the above equations through motion on individual PESs as suggested by Eq. B.9 and incorporates transitions between states via hopping between surfaces with probabilities generated from Eq. 1.8, which is justified by its similarity to Eq. B.8.

Appendix C

FORTRAN SOURCE CODE

MO Orthonormalization, Excitation Energy, Oscillator Strength, Non-adiabatic Coupling Calculation Routine

```
MODULE Params
IMPLICIT NONE
SAVE

INTEGER,PARAMETER :: DBL=SELECTED_REAL_KIND(p=13)
INTEGER :: basis, steps, occ, states, icon, tots
REAL(kind=DBL) :: excite, width, upper, lower
REAL(kind=DBL) :: ts, maxen

END MODULE Params

PROGRAM SH_prep
USE Params
IMPLICIT NONE

INTEGER :: i, j, k, l, m
INTEGER :: n1, n2
INTEGER, ALLOCATABLE :: MOi(:)
INTEGER, ALLOCATABLE :: MOf(:)
INTEGER, ALLOCATABLE :: IS(:)
```

```
INTEGER :: maxMO
REAL(kind=DBL), ALLOCATABLE :: MOen(:)
REAL(kind=DBL), ALLOCATABLE :: MOco(:,:)
REAL(kind=DBL), ALLOCATABLE :: MOco2(:,:)
REAL(kind=DBL), ALLOCATABLE :: AOdip(:,:)
REAL(kind=DBL), ALLOCATABLE :: DC(:)
REAL(kind=DBL), ALLOCATABLE :: CDC(:,:)
REAL(kind=DBL), ALLOCATABLE :: MOdip(:,:)
REAL(kind=DBL), ALLOCATABLE :: OS(:)
REAL(kind=DBL), ALLOCATABLE :: KSex(:)
REAL(kind=DBL), ALLOCATABLE :: NAC(:,:)

OPEN(UNIT=110,FILE='input_params.dat',ACTION='READ')
READ(110,*) basis
READ(110,*) occ
READ(110,*) steps
READ(110,*) ts
READ(110,*) excite
READ(110,*) width
READ(110,*) icon
READ(110,*) tots
READ(110,*) maxen
CLOSE(110)
states=occ*(basis-occ)
upper=excite+width
lower=excite-width
ALLOCATE(MOen(basis))
```

```
ALLOCATE(MOco(basis,basis))
ALLOCATE(MOco2(basis,basis))
ALLOCATE(AOdip(basis,basis))
ALLOCATE(DC(basis))
ALLOCATE(CDC(basis,basis))
ALLOCATE(MOdip(occ+1:basis,occ))
ALLOCATE(OS(states))
ALLOCATE(KSex(states))
ALLOCATE(MOi(states))
ALLOCATE(MOf(states))
ALLOCATE(IS(steps))
ALLOCATE(NAC(basis,basis))

OPEN(UNIT=120,FILE='AEvals',ACTION='READ')
OPEN(UNIT=130,FILE='AEvecs',ACTION='READ')
OPEN(UNIT=140,FILE='AO_dipole',ACTION='READ')
OPEN(UNIT=210,FILE='KS_abs.dat',ACTION='WRITE')
OPEN(UNIT=220,FILE='KS_ex_en.dat',ACTION='WRITE')
OPEN(UNIT=230,FILE='KS_ex_el.dat',ACTION='WRITE')
OPEN(UNIT=240,FILE='KS_ex_hole.dat',ACTION='WRITE')
OPEN(UNIT=250,FILE='KS_init_state.dat',ACTION='WRITE')
OPEN(UNIT=260,FILE='MO_nacs.dat',ACTION='WRITE')
!Loop over time steps
DO i=1,steps
 READ(120,*) MOen(:)
!k corresponds to the column in the input file
!j corresponds to the row in the input file
```

```
!READ statement without loops would transpose
!the matrix, as compared with the input file
 IF (i==1) THEN
  READ(130,*) ((MOco(j,k),k=1,basis),j=1,basis)
 ELSE
  MOco(:,:)=MOco2(:,:)
 END IF
 READ(130,*) ((MOco2(j,k),k=1,basis),j=1,basis)
 CALL ORTHO(i,MOco,MOco2)
!Loop over three components of dipole matrix
 IF (i<=icon) THEN
  MOdip=0.D0
  DO j=1,3
   READ(140,*) ((AOdip(k,l),l=1,basis),k=1,basis)
!We have the AO dipole matrix and need to MO one
!We have to calculate C+.D.C
   CDC=MATMUL(TRANSPOSE(MOco),MATMUL(AOdip,MOco))
   MOdip=MOdip+(CDC(occ+1:basis,1:occ)**2)
  END DO!AO dipole component loop
 END IF
!In atomic units OS is f_{kl}=(2/3)*(E_{k}-E_{l})*mu_{kl}^2
!f_{kl} is for transition from MO l to MO k
!MOdip(k,l)=mu_{kl}^2
 m=1
 DO k=occ+1,basis
  DO l=1,occ
   IF ((MOen(k)-MOen(l))>maxen) CYCLE
```

```
      IF (i<=icon) THEN
       OS(m)=(2.D0/3.D0)*(MOen(k)-MOen(l))*MOdip(k,l)
      END IF
      KSex(m)=MOen(k)-MOen(l)
      MOi(m)=l
      MOf(m)=k
      m=m+1
    END DO
  END DO
  m=m-1
!Sort results according to excitation energy
  CALL SORT(i,m,KSex,OS,MOi,MOf,IS)
!Calculate non-adiabatic coupling via
!d_{jk}=(1/(2ts))*[<Y_{j}(t)|Y_{k}(t+ts)> - <Y_{j}(t+ts)|Y_{k}(t)>]
!in atomic units, where ts is the time step and Y are the MOs
  NAC=(1.D0/(2.D0*ts))*(MATMUL(TRANSPOSE(MOco),MOco2)- &
    MATMUL(TRANSPOSE(MOco2),MOco))
!Print results
  IF (i<=icon) THEN
    WRITE(250,*) IS(i)
  END IF
! DO j=1,states
  DO j=1,tots
    IF (i<=icon) THEN
      WRITE(210,'(2ES14.5)') KSex(j), OS(j)
    END IF
    WRITE(220,'(ES19.10)') KSex(j)
```

```
   WRITE(230,'(I4)') MOf(j)
   WRITE(240,'(I4)') MOi(j)
  END DO
  IF (MAXVAL(MOf(1:tots))>maxMO) THEN
   maxMO=MAXVAL(MOf(1:tots))
  END IF
  IF (i==steps) THEN
   WRITE(*,*) maxMO
  END IF
  IF (i<=icon) THEN
   WRITE(210,*)
  END IF
  DO j=1,basis
   DO k=1,basis
    WRITE(260,'((ES19.10),$)') NAC(j,k)
   END DO
   WRITE(260,*)
  END DO
END DO!step loop
CLOSE(120)
CLOSE(130)
CLOSE(140)
CLOSE(210)
CLOSE(220)
CLOSE(230)
CLOSE(240)
CLOSE(250)
```

```
CLOSE(260)
END PROGRAM SH_prep

SUBROUTINE SORT(spot,num,A,B,C,D,E)
USE Params
IMPLICIT NONE

INTEGER :: i, j, itemp
INTEGER, INTENT(IN) :: spot, num
REAL(kind=DBL), DIMENSION(states), INTENT(IN OUT) :: A
REAL(kind=DBL), DIMENSION(states), INTENT(IN OUT) :: B
INTEGER, DIMENSION(states), INTENT(IN OUT) :: C
INTEGER, DIMENSION(states), INTENT(IN OUT) :: D
INTEGER, DIMENSION(steps), INTENT(IN OUT) :: E
REAL(kind=DBL) :: temp, temp2

temp2=0.D0
DO i=1,num-1
 DO j=i+1,num
  IF (A(j)<A(i)) THEN
   temp=A(j)
   A(j)=A(i)
   A(i)=temp
   temp=B(j)
   B(j)=B(i)
   B(i)=temp
   temp=C(j)
```

```
      C(j)=C(i)
      C(i)=temp
      temp=D(j)
      D(j)=D(i)
      D(i)=temp
    END IF
  END DO
  IF (spot<=icon) THEN
    IF (A(i)>=lower .AND. A(i)<=upper) THEN
      IF(B(i)>temp2) THEN
        temp2=B(i)
        itemp=i
      END IF
    END IF
  END IF
END DO
IF (spot<=icon) THEN
  E(spot)=itemp
END IF

END SUBROUTINE SORT

SUBROUTINE ORTHO(spot,M1,M2)
USE Params
IMPLICIT NONE

INTEGER :: LDA
```

```
INTEGER :: LWORK
CHARACTER, PARAMETER :: JOBZ = 'V'
CHARACTER, PARAMETER :: UPLO = 'U'
INTEGER :: i, j, INFO
INTEGER, INTENT(IN) :: spot
REAL(kind=DBL), DIMENSION(3*basis-1) :: WORK
REAL(kind=DBL), DIMENSION(basis) :: W1, W2
REAL(kind=DBL), DIMENSION(basis,basis), INTENT(IN OUT) :: M1, M2
REAL(kind=DBL), DIMENSION(basis,basis) :: S1, S2, E1, E2

LDA=basis
LWORK=3*basis-1
IF (spot==1) THEN
 S1=MATMUL(TRANSPOSE(M1),M1)
 CALL DSYEV(JOBZ,UPLO,basis,S1,LDA,W1,WORK,LWORK,INFO)
 E1=0.D0
 DO i=1,basis
  E1(i,i)=1.D0/SQRT(W1(i))
 END DO
 M1=MATMUL(M1,MATMUL(S1,MATMUL(E1,TRANSPOSE(S1))))
 DO i=1,basis
  M1(:,i)=M1(:,i)/SQRT(DOT_PRODUCT(M1(:,i),M1(:,i)))
 END DO
END IF
S2=MATMUL(TRANSPOSE(M2),M2)
CALL DSYEV(JOBZ,UPLO,basis,S2,LDA,W2,WORK,LWORK,INFO)
E2=0.D0
```

```
DO i=1,basis
  E2(i,i)=1.D0/SQRT(W2(i))
END DO
M2=MATMUL(M2,MATMUL(S2,MATMUL(E2,TRANSPOSE(S2))))
DO i=1,basis
  M2(:,i)=M2(:,i)/SQRT(DOT_PRODUCT(M2(:,i),M2(:,i)))
END DO

END SUBROUTINE ORTHO
```

Surface Hopping Routine

```
MODULE stats
IMPLICIT NONE
INTEGER, PARAMETER :: DBL = SELECTED_REAL_KIND(p=13)
INTEGER :: states, sh_time, m_flag, num_traj
INTEGER :: init_cond, high, steps, conds, init_state
INTEGER :: basis, inactive
REAL(kind=DBL) :: e_step, n_step, temper
REAL(kind=DBL), ALLOCATABLE :: epi(:,:,:), nac(:,:,:)
END MODULE stats

PROGRAM SH_slater
USE stats
IMPLICIT NONE

!Declare Variables/Constants
INTEGER :: state_now, state_prev, ntime, etime, mark
INTEGER :: traj, i, j, k, l, h_test, ratio, current
```

```
CHARACTER(7) :: file_name
REAL(kind=DBL) :: zeta, trace, beta
REAL(kind=DBL) :: boltz
COMPLEX(kind=DBL), PARAMETER :: eye = (0.D0, 1.D0)
REAL(kind=DBL), PARAMETER :: hbar = 6.58211928D-1
REAL(kind=DBL), DIMENSION(3) :: prefac
REAL(kind=DBL), DIMENSION(4) :: pref2
INTEGER, ALLOCATABLE :: state(:)
REAL(kind=DBL), ALLOCATABLE :: hop(:), hp_f(:,:), pops(:,:)
REAL(kind=DBL), ALLOCATABLE :: eslope(:,:), nslope(:,:)
COMPLEX(kind=DBL), ALLOCATABLE :: den_now(:,:), den_next(:,:)
COMPLEX(kind=DBL), ALLOCATABLE :: den_temp(:,:), kd(:,:)
REAL(kind=DBL), ALLOCATABLE :: int_a(:,:)

CALL get_size()
prefac(1)=0.5D0
prefac(2)=0.5D0
prefac(3)=1.D0
pref2(1)=e_step/6.D0
pref2(2)=e_step/3.D0
pref2(3)=e_step/3.D0
pref2(4)=e_step/6.D0
steps=INT(REAL(sh_time)/n_step)
ratio=INT((n_step)/e_step)-1
beta=1.D0/(8.6173324D-5*temper)
ALLOCATE(nac(states,states,steps+1))
ALLOCATE(epi(states,states,steps+1))
```

```
ALLOCATE(state(num_traj))
ALLOCATE(hop(states))
ALLOCATE(pops(states,steps+1))
ALLOCATE(hp_f(states,states))
ALLOCATE(nslope(states,states))
ALLOCATE(eslope(states,states))
ALLOCATE(den_now(states,states))
ALLOCATE(den_next(states,states))
ALLOCATE(den_temp(states,states))
ALLOCATE(kd(states,states))
ALLOCATE(int_a(states,states))
mark=0
IF (MODULO(REAL(sh_time),n_step)/=0.D0) THEN
 WRITE(*,*) 'Trajectory time and nuclear step size are not compatable!'
 STOP
END IF
OPEN(UNIT=9,FILE='KS_ex_en.dat',STATUS='OLD',ACTION='READ')
OPEN(UNIT=19,FILE='MO_nacs.dat',STATUS='OLD',ACTION='READ')
OPEN(UNIT=39,FILE='KS_init_state.dat',STATUS='OLD',ACTION='READ')
OPEN(UNIT=59,FILE='KS_ex_hole.dat',STATUS='OLD',ACTION='READ')
OPEN(UNIT=69,FILE='KS_ex_el.dat',STATUS='OLD',ACTION='READ')

DO i=1,init_cond-1
 DO j=1,states+inactive-1
  READ(9,*)
  READ(59,*)
  READ(69,*)
```

```
 END DO
 DO j=1,basis
  READ(19,*)
 END DO
END DO
Master:DO i = init_cond, conds+init_cond-1
 WRITE(file_name,'(A,I3.3)') 'out.',i
 OPEN(UNIT=109,FILE=file_name,STATUS='NEW',ACTION='WRITE')
 pops=0.D0
 REWIND(39)
 DO j=init_cond,i-1
  READ(39,*)
 END DO
 READ(39,*) init_state
 CALL ennac(i)

 den_now=(0.D0,0.D0)
 den_now(init_state+1,init_state+1)=(1.D0,0.D0)
 den_next=den_now
 state=init_state+1
 pops(init_state+1,1)=pops(init_state+1,1)+(1.D0*REAL(num_traj,DBL))

!Begin Calculation
 NProp:DO ntime = 1, steps
  EProp:DO etime = 0, ratio
   IF (etime==0) THEN
    int_a=-2.D0*REAL(den_now,DBL)*nac(:,:,ntime)
```

```
    END IF
    trace=0.D0
    den_temp=den_now
    eslope=(REAL(etime,DBL)/ &
     REAL(ratio,DBL))*(epi(:,:,ntime+1)-epi(:,:,ntime))
    nslope=(REAL(etime,DBL)/ &
     REAL(ratio,DBL))*(nac(:,:,ntime+1)-nac(:,:,ntime))
    RK4:DO j=1,4
!   RK4 slopes for the density matrix
     kd=MATMUL((-(eye/hbar)*(epi(:,:,ntime)+eslope)- &
        (nac(:,:,ntime)+nslope)),den_temp)- &
       MATMUL(den_temp,(-(eye/hbar)*(epi(:,:,ntime)+eslope)- &
         (nac(:,:,ntime)+nslope)))
     IF (j<4) THEN
      den_temp=den_now+e_step*prefac(j)*kd
     END IF
     den_next=den_next+pref2(j)*kd
     kd=(0.D0,0.D0)
    END DO RK4
    DO j=1,states
     trace=trace+ABS(den_next(j,j))
    END DO
    IF (etime==((ratio+1)/2)) THEN
     int_a=int_a+4.D0*(-2.D0*REAL(den_next,DBL)* &
      ((nac(:,:,ntime)+nac(:,:,ntime+1))/2.D0))
    END IF
    IF (etime==ratio) THEN
```

```
      int_a=int_a -2.D0*REAL(den_next ,DBL)*nac(:,:,ntime+1)
     END IF
     den_now=den_next
    END DO EProp
  ! Calculate hopping probabilities for each state
    IF (m_flag==2) THEN
     DO j=1, states
      DO k=1, states
       IF (k>j) THEN
        boltz=exp(-beta*(epi(k,k,ntime+1)-epi(j,j,ntime+1)))
       ELSE
        boltz=1.D0
       END IF
       hp_f(j,k)=MAX(0.D0, boltz*((REAL(n_step ,DBL)/6.D0)*(int_a(k,j)))/ &
        ABS(den_next(j,j)))
      END DO
      hp_f(j,j)=0.D0
     END DO
    END IF
    DO traj = 1, num_traj
  !  Test for a hop against random number
     IF (m_flag==2) THEN
      CALL RANDOM_NUMBER(zeta)
      hop=0.D0
      h_test=0
      current=state(traj)
      hop_prob2:DO j = 1, states
```

```
      DO k = 1, j
        hop(j)=hop(j)+hp_f(current,k)
      END DO
      IF (h_test==1) EXIT hop_prob2
      IF (hop(j)>zeta) THEN
        h_test=1
        state(traj)=j
      END IF
     END DO hop_prob2
     h_test=0
    END IF
    IF (m_flag==3) THEN
     DO j = 1, states
      pops(j,ntime+1)=pops(j,ntime+1)+ABS(den_next(j,j))
     END DO
    ELSE
     pops(state(traj),ntime+1)=pops(state(traj),ntime+1)+1.D0
    END IF
  END DO
END DO NProp ! nuclear propagation loop

WRITE(109,'(A,I5.5)') 'init_state=', init_state+1
WRITE(109,'(A,I5.5)') '#traj=', num_traj
WRITE(109,*) '--------------------'
WRITE(109,'((A),$)') 't(fs)    '
DO j = 1, states
 WRITE(109,'((A,I3.3,A),$)') '**Pop(',j,')**    '
```

```
 END DO
 WRITE(109,*)
 DO j = 1, steps+1
  WRITE(109,'((F5.1),$)') REAL(j-1)*n_step
  DO k = 1, states
   WRITE(109,'((ES15.6),$)') pops(k,j)/REAL(num_traj,DBL)
  END DO
  WRITE(109,*)
 END DO
 CLOSE(UNIT=109)
END DO Master
CLOSE(UNIT=39)
CLOSE(UNIT=9)
CLOSE(UNIT=19)
CLOSE(UNIT=59)
CLOSE(UNIT=69)
CLOSE(UNIT=209)

END PROGRAM SH_slater

SUBROUTINE get_size
USE stats
OPEN(UNIT=8,FILE='input.dat',STATUS='OLD',ACTION='READ')
READ(8,*) m_flag
READ(8,*) states
READ(8,*) inactive
READ(8,*) high
```

```
READ(8,*) basis
READ(8,*) init_cond
READ(8,*) conds
READ(8,*) num_traj
READ(8,*) sh_time
READ(8,*) n_step
READ(8,*) e_step
READ(8,*) temper
END SUBROUTINE get_size

SUBROUTINE ennac(ns)
USE stats
IMPLICIT NONE
CHARACTER(9) :: filename
INTEGER, INTENT(IN) :: ns
INTEGER :: i, j, k, stat
INTEGER, DIMENSION(states-1) :: ks1, ks2
REAL(kind=DBL), DIMENSION(states-1) :: etemp1
REAL(kind=DBL), DIMENSION(high,high) :: vtemp1


IF (ns==init_cond) THEN
 DO i=1,steps+1
  READ(9,*) etemp1
  DO j=1,inactive
   READ(9,*)
  END DO
```

```
    epi(1,1,i)=0.D0
    DO j=2,states
      epi(j,j,i)=2.71165D1*etemp1(j-1)
    END DO
  END DO
ELSE
  DO i=1,steps
    epi(:,:,i)=epi(:,:,i+1)
  END DO
  READ(9,*) etemp1
  DO j=1,inactive
    READ(9,*)
  END DO
  epi(1,1,steps+1)=0.D0
  DO j=2,states
    epi(j,j,steps+1)=2.71165D1*etemp1(j-1)
  END DO
END IF

IF (ns==init_cond) THEN
  DO i=1,steps+1
    DO j=1,high
      READ(19,*) (vtemp1(j,k),k=1,high)
    END DO
    DO j=1,basis-high
      READ(19,*)
    END DO
```

```
   READ(59,*) ks1
   READ(69,*) ks2
   DO j=1,inactive
    READ(59,*)
    READ(69,*)
   END DO
   DO j=2,states
    nac(1,j,i)=vtemp1(ks1(j-1),ks2(j-1))
    nac(j,1,i)=vtemp1(ks2(j-1),ks1(j-1))
    DO k = 2, states
     IF (ks1(j-1)==ks1(k-1) .AND. ks2(j-1)/=ks2(k-1)) THEN
      nac(j,k,i)=vtemp1(ks2(j-1),ks2(k-1))
     ELSE IF (ks1(j-1)/=ks1(k-1) .AND. ks2(j-1)==ks2(k-1)) THEN
      nac(j,k,i)=-vtemp1(ks1(j-1),ks1(k-1))
     ELSE
      nac(j,k,i)=0.D0
     END IF
    END DO
   END DO
  END DO
 ELSE
  DO i=1,steps
   nac(:,:,i)=nac(:,:,i+1)
  END DO
  DO j=1,high
   READ(19,*) (vtemp1(j,k),k=1,high)
  END DO
```

```
 DO j=1,basis-high
  READ(19,*)
 END DO
 READ(59,*) ks1
 READ(69,*) ks2
 DO j=1,inactive
  READ(59,*)
  READ(69,*)
 END DO
 DO j = 2, states
  nac(1,j,steps+1)=vtemp1(ks1(j-1),ks2(j-1))
  nac(j,1,steps+1)=vtemp1(ks2(j-1),ks1(j-1))
  DO k = 2, states
   IF (ks1(j-1)==ks1(k-1) .AND. ks2(j-1)/=ks2(k-1)) THEN
    nac(j,k,steps+1)=vtemp1(ks2(j-1),ks2(k-1))
   ELSE IF (ks1(j-1)/=ks1(k-1) .AND. ks2(j-1)==ks2(k-1)) THEN
    nac(j,k,steps+1)=-vtemp1(ks1(j-1),ks1(k-1))
   ELSE
    nac(j,k,steps+1)=0.D0
   END IF
  END DO
 END DO
END IF

END SUBROUTINE ennac
```